JCTC Journal of Chemical Theory and Computation

pubs.acs.org/JCTC Article

Cherry-Picking Resolvents: Recovering the Valence Contribution in X-ray Two-Photon Absorption within the Core−Valence-Separated Equation-of-Motion Coupled-Cluster Response Theory

Josefine H. Andersen,[§] Kaushik D. Nanda,*[,§] Anna I. Krylov,* and Sonia Coriani*

Cite This: J. Chem. Theory Comput. 2022, 18, 6189−6202 Read Online

ACCESS | Metrics & More | Article Recommendations | Supporting Information

ABSTRACT: Calculations of first-order response wave functions in the X-ray regime often diverge within correlated frameworks such as equation-of-motion coupled-cluster singles and doubles (EOM-CCSD), a consequence of the coupling with the valence ionization continuum. Here, we extend our strategy of introducing a hierarchy of approximations to the EOM-EE-CCSD resolvent (or, inversely, the model Hamiltonian) involved in the response equations for the calculation of X-ray two-photon absorption (X2PA) cross sections. We exploit the frozen-core core−valence separation (fc-CVS) scheme to first decouple the core and valence Fock spaces, followed by a separate approximate treatment of the valence resolvent. We demonstrate the robust convergence of X-ray response calculations within this framework and compare X2PA spectra of small benchmark molecules with the previously reported density functional theory results.

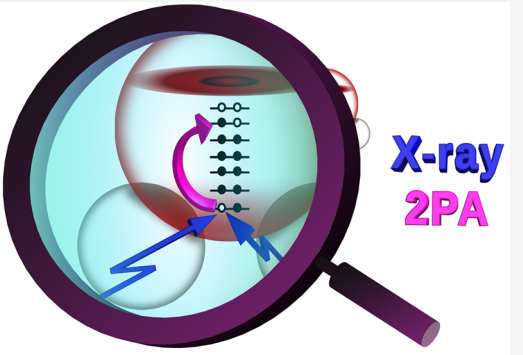

1. INTRODUCTION

Correlated electronic-structure methods, such as those based on coupled-cluster (CC) theory, provide a robust platform for computing ground and excited states in a variety of closed- and open-shell systems. The scope of molecules that can be treated by these high-level methods is expanding, thanks to advances in algorithmic strategies and computing hardware. In the past three decades, CC methods such as the equation-of-motion coupled-cluster[1−3] (EOM-CC) and the coupled-cluster response[4,5] (CC-RSP) theories have been vigorously developed to afford computations of an ever-growing list of molecular properties,[6] greatly enhancing our capabilities for reliable first-principles modeling of spectroscopic experiments. These methods are now routinely employed for computing ground- and excited-state properties in linear and nonlinear regimes. Examples of nonlinear properties include multiphoton absorption cross sections,[7−9] inelastic scattering cross sections,[10−13] first and second hyperpolarizabilities,[14−17] excited-state polarizabilities[18,19] and multiphoton transition moments between excited states,[20] multiphoton and magnetic circular dichroism strengths,[21−24] and *g*-tensors,[25] to mention just a few. In addition, the high-level CC methods provide the gold standard for benchmarking approximate and computationally less expensive methods, such as those based on density functional theory (DFT), which can treat much larger systems. Concomitant developments of embedding schemes[26−30] have afforded robust CC condensed-phase modeling of molecular processes and properties in solutions, protein environments, and periodic systems. Further, advances in orbital concepts[17,31−36] and wave function analysis tools[37−40] have facilitated robust molecular-level understanding of the molecular processes within the framework of correlated methods.

The EOM-CC theory offers a powerful single-reference framework for computing a variety of electronic states: excited states, ionized states, electron-attached states, and so on. The level of correlation treatment can be systematically improved following the hierarchy of CC/EOM-CC approximations (CC2, CCSD, CC3, CCSDT, ...) up to the exact limit. A crucially important trait of this framework is its flexibility in the choice of the EOM operators and the reference Slater determinant, which are adapted to provide a balanced treatment of the set of target states. EOM-CC and CC-RSP formalisms produce the same excitation energies, but they can differ in their treatment of state and transition properties.[6,41] The EOM-CC framework allows for the description of properties as generalized expectation values that are obtained by parametrizing exact expressions using eigenenergies and left and right eigenvectors of the (non-Hermitian) similarity-transformed EOM-CC Hamiltonian. EOM-CC response properties within this "expectation-value approach" are identical to the response properties derived from the coupled-cluster configuration interaction (CC-CI) model,

Received: May 23, 2022
Published: September 9, 2022

https://doi.org/10.1021/acs.jctc.2c00541
J. Chem. Theory Comput. 2022, 18, 6189−6202

where the time-dependent Schrödinger equation is solved using an exponential parametrization to describe the unperturbed system and a linear parametrization to describe the time evolution of the unperturbed system.[42]

In CC (and CC-CI) response theory, the expressions for properties are given by derivatives of appropriate (quasi)energy Lagrangians with respect to the strength of the external perturbation(s)[6,7,20,43,44] or, equivalently, from the response of a generalized time-dependent expectation value of a time-independent one-electron operator.[4] Note that properties computed within the alternative analytic-derivative EOM-CC approach, involving derivatives of (quasi)energy Lagrangians with respect to the strength of the external perturbation(s), are identical to those from CC-RSP.[19,45,46] CC-RSP requires additional response intermediates for computing multiphoton absorption moments, relative to the EOM-CC expectation-value approach.[5,7] The EOM-CC expectation-value approach for properties becomes exact in the limit of full configuration interaction. This parametrization ensures that the pole structures of frequency-dependent properties are not spoiled by artificial poles, which may negatively impact higher-order excited state properties computed with the CC-RSP approach.[19]

This paper presents a new extension of EOM-CC theory for modeling two-photon absorption (2PA) cross sections in the X-ray regime (X2PA). This development is motivated by the need for robust and accurate tools for modeling X2PA processes, which occur in experiments involving intense X-ray radiation sources such as X-ray free-electron lasers[47−52] (XFEL). Similarly to the UV−vis domain, X2PA has different selection rules compared to one-photon X-ray absorption (XAS) and could, therefore, deliver complementary information. X2P techniques combine the advantages of core−electron transitions with those of standard 2P techniques: the quadratic dependence on intensity endows 2P techniques with better spatial resolution, whereas core-level transitions afford elemental and orbital sensitivity to the local environment and oxidation states. On the downside, in the high-intensity regime, X2PA is competing against a slew of single-photon and sequential multiphoton processes, such as core photoionization, stimulated emission, and scattering, which complicates the interpretation of the experimental observations.[48,52] So far, the published experimental papers have focused on transition metals.[48,52] Competing processes such as photoionization and molecular fragmentation have hampered experiments on small molecules.

In view of the high activity in experimental nonlinear X-ray spectroscopies, the paucity of robust *ab initio* methods capable of describing the underlying nonlinear properties limits the potential impact of new experimental techniques, especially given the above-mentioned contributions from competing processes in the experimental signal. Being the simplest higher-order process from the theoretical point of view, X2PA can serve as a platform for future developments of theoretical methods for modeling higher-order multiphoton processes, such as X-ray sum-frequency generation[53−55] and X-ray second-harmonic generation.[56,57]

2PA cross sections can be computed using different approaches. Formally, 2PA moments can be obtained from the first residues of quadratic response functions (first electric-dipole hyperpolarizability tensor) to build the 2PA strength tensor and cross sections.[7,58−60] Alternatively, elements of the 2PA strength tensor can be evaluated as first residues of the cubic response functions (second electric-dipole hyperpolarizability tensor).[7,9,10,58−60] In practice, these relationships are exploited in the resonance convergent complex polarization propagator (CPP) approach[61] and in damped response theory.[6,62] In these approaches, a phenomenological imaginary inverse lifetime (damping) parameter is introduced to compute the 2PA strengths from the imaginary part of the cubic response function. The CPP approach has been exploited within the framework of time-dependent DFT (TD-DFT) for computing both valence 2PA[63] and X2PA spectra.[64] Reference 64 by Fahleson et al. is the only published theoretical work on X2PA until now. Here, we explore a computational strategy based on the many-body EOM-CC framework.

CC-RSP[7,8] and EOM-CC expectation-value[9] frameworks have also been developed for computing valence 2PA cross sections; the latter employs first-order response wave functions to compute the EOM-CC-parameterized exact sum-over-states expressions for the 2PA moments.[9] Within the EOM-CC framework, an implementation based on damped response theory also exists (unreported[65]), which computes complex-valued 2PA moments following the introduction of the phenomenological damping for avoiding divergences in modeling doubly resonant 2PA processes. However, the extension of the EOM-CC formalism for computing valence 2PA to X2PA is not straightforward.

In X2PA transitions (Figure 1), the final states are core-excited states. Such states are high-lying and, therefore, difficult to compute with standard numerical solvers. Moreover, these states are Feshbach resonances embedded in the valence ionization continuum. As a result, standard correlated methods designed for computing electronically bound states cannot be used for these resonances, whose wave functions are not L^2-integrable.[66−69] Without special modifications, attempts to compute core-excited states with these methods are plagued by the erratic (often, divergent) behavior of solvers, a lack of systematic convergence with basis-set increase, and, often, unphysical solutions.[12,13,70,71] This issue is effectively addressed by the core−valence separation (CVS) approach[72] in which the core resonances are decoupled from the valence continuum by removing the purely valence-excited determinants from the EOM-CC configuration space. This pruning of the Fock space makes the core-level states artificially bound in the computation, leading to convergent results. The errors in energies introduced due to the CVS dilution of dynamical correlation in methods such as EOM-CC are typically of the order of less than 1 eV.[73,74] The effect of the continuum can be reincorporated, e.g., via a perturbative approach[73,75] or via the Feshbach−Fano formalism.[76,77] Further, the CVS treatment is not state specific, so multiple states can be computed simultaneously, just as in the case of standard EOM-CC calculations; this feature is attractive in the context of spectroscopy modeling.

Within the CC domain, the CVS scheme was pioneered by Coriani and Koch[73,75] for computing core-excitation energies (and spectral intensities) as well as core-ionization energies. Since then, the CVS strategy has been used in several CC-RSP and EOM-CC frameworks,[73,74,78,79] enabling the modeling of XAS, XPS, XCD, and XES spectra.[11,80−82] The theory was further extended to higher-order properties such as resonant inelastic X-ray scattering (RIXS) cross sections.[11−13] Similar to 2PA, RIXS is a two-photon process; RIXS moments are also formally given by sum-over-states (SOS) expressions within the EOM-CC expectation-value framework. In practical calculations, the SOS expressions are recast into closed-form expressions by using first-order response wave functions. The RIXS response calculations for these wave functions are affected

https://doi.org/10.1021/acs.jctc.2c00541
J. Chem. Theory Comput. 2022, 18, 6189−6202

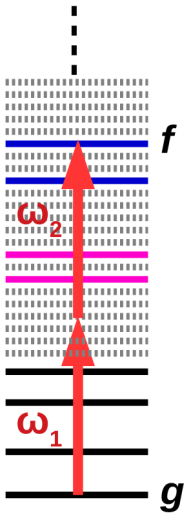

Figure 1. In X2PA, two X-ray photons of energies ω_1 and ω_2 are coherently absorbed such that $\omega_1 + \omega_2$ equals the excitation energy $E_f - E_g$ of the final state f that is core excited relative to the initial state g. The X2PA moments have contributions from all states of the system, including the ground and bound valence-excited states (black lines), core-excited states (blue lines), valence resonances (magenta lines), and valence continuum states (ultrafine gray dashes).

by their coupling with the continuum, and CVS has been recently adapted to deal with this issue.[11−13] The limitations of straightforward application of CVS and possible extensions have been discussed in ref 13, giving rise to series of approximations such as CVS-0, CVS-uS, etc. (see section 2.3).

In this contribution, we explore the performance of the CVS-uS approach for computing X2PA cross sections within the EOM-CC singles and doubles framework for electronic excitations (EOM-EE-CCSD). We compare the X2PA spectra computed with the CVS-0 and CVS-uS approaches for small benchmark molecules to highlight the importance of including the valence contribution for modeling X2PA. We also compare these computed X2PA spectra with those from ref 64.

2. THEORY

To distinguish between the canonical EOM-EE-CCSD and fc-CVS-EOM-EE-CCSD methods, we use different symbols below. The calligraphic symbols, $\mathcal{H}$, $\mathcal{T}$, $\mathcal{L}$, $\mathcal{R}$, $\mathcal{E}$, $\mathcal{X}$, and $\mathcal{G}$, are associated with the canonical EOM-EE-CCSD method, and regular symbols, H, T, L, R, E, X, and G, are associated with the fc-CVS-EOM-EE-CCSD method.

2.1. The CVS EOM-EE-CCSD Method. The EOM-EE-CCSD method describes the right ($\hat{\mathcal{R}}|\Phi_0\rangle$) and left ($\langle\Phi_0|\hat{\mathcal{L}}$) wave functions of target states according to the eigenvalue equations

$$\hat{\bar{\mathcal{H}}}\hat{\mathcal{R}}^k|\Phi_0\rangle = \mathcal{E}_k\hat{\mathcal{R}}^k|\Phi_0\rangle \tag{1}$$

and

$$\langle\Phi_0|\hat{\mathcal{L}}^k\bar{\mathcal{H}} = \langle\Phi_0|\hat{\mathcal{L}}^k\mathcal{E}_k \tag{2}$$

where $\hat{\bar{\mathcal{H}}} = e^{-\hat{\mathcal{T}}}\hat{\mathcal{H}}e^{\hat{\mathcal{T}}}$ is the similarity-transformed EOM-EE-CCSD Hamiltonian, $\mathcal{E}_k$ is the energy of the target state k, and $\hat{\mathcal{T}}$ is the CC operator satisfying the CC equations

$$\langle\Phi_0|\hat{\bar{\mathcal{H}}}|\Phi_0\rangle = \mathcal{E}_0; \quad \langle\Phi_\nu|\hat{\bar{\mathcal{H}}}|\Phi_0\rangle = 0 \tag{3}$$

Here, $\mathcal{E}_0$ is the energy of the CCSD state defined by the reference determinant Φ_0, and Φ_ν are the singly and doubly excited determinants relative to Φ_0. The operators $\hat{\mathcal{T}}$, $\hat{\mathcal{R}}$, and $\hat{\mathcal{L}}$ are given in terms of creation ($a^\dagger$, $b^\dagger$) and annihilation (i, j) operators as follows:

$$\hat{\mathcal{T}} = \hat{\mathcal{T}}_1 + \hat{\mathcal{T}}_2; \quad \hat{\mathcal{T}}_1 = \sum_{ia} t_i^a a^\dagger i; \quad \hat{\mathcal{T}}_2 = \sum_{ijab} t_{ij}^{ab} a^\dagger b^\dagger ji \tag{4}$$

$$\hat{\mathcal{R}} = r_0 + \hat{\mathcal{R}}_1 + \hat{\mathcal{R}}_2; \quad \hat{\mathcal{R}}_1 = \sum_{ia} r_i^a a^\dagger i; \quad \hat{\mathcal{R}}_2 = \sum_{ijab} r_{ij}^{ab} a^\dagger b^\dagger ji \tag{5}$$

and

$$\hat{\mathcal{L}} = l_0 + \hat{\mathcal{L}}_1 + \hat{\mathcal{L}}_2; \quad \hat{\mathcal{L}}_1 = \sum_{ia} l_i^a i^\dagger a; \quad \hat{\mathcal{L}}_2 = \sum_{ijab} l_{ij}^{ab} i^\dagger j^\dagger ba \tag{6}$$

For the CCSD state, $\hat{\mathcal{R}} = r_0 = 1$ and $\hat{\mathcal{L}} = 1 + \hat{\Lambda}$, where $\hat{\Lambda} = \hat{\Lambda}_1 + \hat{\Lambda}_2$ is the CCSD lambda operator. For EOM-EE-CCSD target states, $l_0 = 0$.

The amplitudes of $\hat{\mathcal{R}}$ and $\hat{\mathcal{L}}$ in eqs 5 and 6 for target states are computed by diagonalizing $\hat{\bar{\mathcal{H}}}$ in the space of the reference, singly excited, and doubly excited determinants using standard techniques such as the generalized Davidson procedure. Whereas such strategies are effective for computing low-lying excited states, their straightforward application to obtain high-lying core-excited states is impractical.[83] Further, the presence of the valence continuum and the diagonal preconditioner being inappropriate for the doubles−doubles block of the Hamiltonian result in erratic behavior of such calculations of core-level states. For computing core-excited states, the core-excited block of $\hat{\bar{\mathcal{H}}}$, defined by omitting the reference and purely valence-excited determinants from the configuration space, is diagonalized instead of $\hat{\bar{\mathcal{H}}}$. In ref 13 and this study, we call this block the CVS-0 model Hamiltonian $\hat{\bar{H}}^{\text{core}}$. Whereas only the couplings of the core-excited configurations with the purely valence doubly excited configurations are problematic from the convergence viewpoint, the removal of the purely valence singly excited determinants makes the spectrum of the CVS-0 Hamiltonian be that of purely core-excited states. This is an attractive feature as it enables direct calculations of the lowest core-excited states without a significant loss of dynamical correlation. We denote the EOM-EE-CCSD operators that diagonalize $\hat{\bar{H}}^{\text{core}}$ as $\hat{R}^{\text{core}}$ and $\hat{L}^{\text{core}}$.

Here, we compute the ground and valence-excited states with (specific) core electrons frozen. Hence, these states (and, therefore, CCSD $\hat{T}$ and the corresponding EOM-EE-CCSD $\hat{R}^{\text{val}}$ and $\hat{L}^{\text{val}}$ amplitudes) are computed in the configuration space spanning the reference and purely valence-excited determinants only. Therefore, in our frozen-core (fc) CVS-EOM-EE-CCSD model, the valence-excitation space is uncoupled to the core-excitation space by construction. This is in contrast to the CVS model from ref 73, where the two spaces are decoupled by applying dedicated projectors. Our strategy for computing X2PA spectra is general and applicable to both of these variants of CVS-EOM-EE-CCSD. We refer to the Hamiltonian block defined by the reference and valence-excited determinants as

https://doi.org/10.1021/acs.jctc.2c00541
J. Chem. Theory Comput. 2022, 18, 6189−6202

$\hat{\bar{H}}^{\mathrm{val}}$. The fc-CVS-EOM-EE-CCSD Hamiltonian, $\hat{\bar{H}}$, is then block diagonal and made up of $\hat{\bar{H}}^{\mathrm{val}}$ and $\hat{\bar{H}}^{\mathrm{core}}$ blocks.

2.2. 2PA Moments within EOM-EE-CCSD Response Theory. The right and left 2PA moments for transitions between states g and f within exact theory are given by the following sum-over-states expressions:

$$M_{xy}^{f\leftarrow g}(\omega_1, \omega_2) = -\sum_n \left(\frac{\langle \Psi^f|\hat{\mu}_y|\Psi^n\rangle\langle \Psi^n|\hat{\mu}_x|\Psi^g\rangle}{\mathcal{E}_n - \mathcal{E}_g - \omega_1} + \frac{\langle \Psi^f|\hat{\mu}_x|\Psi^n\rangle\langle \Psi^n|\hat{\mu}_y|\Psi^g\rangle}{\mathcal{E}_n - \mathcal{E}_g - \omega_2} \right) \tag{7}$$

and

$$M_{xy}^{g\leftarrow f}(-\omega_1, -\omega_2) = -\sum_n \left(\frac{\langle \Psi^g|\hat{\mu}_x|\Psi^n\rangle\langle \Psi^n|\hat{\mu}_y|\Psi^f\rangle}{\mathcal{E}_n - \mathcal{E}_f + \omega_2} + \frac{\langle \Psi^g|\hat{\mu}_y|\Psi^n\rangle\langle \Psi^n|\hat{\mu}_x|\Psi^f\rangle}{\mathcal{E}_n - \mathcal{E}_f + \omega_1} \right) \tag{8}$$

where ω_1 and ω_2 are the energies of the two photons absorbed such that $\omega_1 + \omega_2 = \mathcal{E}_f - \mathcal{E}_g$, Ψs are the zero-order wave functions, and $\hat{\mu}_x$ ($\hat{\mu}_y$) is the dipole-moment operator along the Cartesian coordinate x (y) $\in \{x, y, z\}$. Within the EOM-EE-CCSD expectation-value approach, eqs 7 and 8 are parameterized by EOM-EE-CCSD wave functions and energies by replacing $\langle\Psi^k|$ with $\langle\Phi_0|\hat{\mathcal{L}}^k \equiv \langle\mathcal{L}^k|$, $|\Psi^k\rangle$ with $\hat{\mathcal{R}}^k|\Phi_0\rangle \equiv |\mathcal{R}^k\rangle$, and $\hat{\mu}$ with the similarity-transformed dipole operator $\hat{\bar{\mu}}$. This EOM-EE-CCSD approach, previously used to compute valence 2PA transitions,[9] then recasts eqs 7 and 8 into closed-form expressions using the first-order response wave function ($|\mathcal{X}_x^k(\omega)\rangle \equiv |\mathcal{X}_x^{k,\omega}\rangle$) as follows:

$$M_{xy}^{f\leftarrow g}(\omega_1, \omega_2) = -(\langle\mathcal{L}^f|\hat{\bar{\mu}}_y|\mathcal{X}_x^{g,\omega_1}\rangle + \langle\mathcal{L}^f|\hat{\bar{\mu}}_x|\mathcal{X}_y^{g,\omega_2}\rangle) \tag{9}$$

and

$$M_{xy}^{g\leftarrow f}(-\omega_1, -\omega_2) = -(\langle\mathcal{L}^g|\hat{\bar{\mu}}_x|\mathcal{X}_y^{f,-\omega_2}\rangle + \langle\mathcal{L}^g|\hat{\bar{\mu}}_y|\mathcal{X}_x^{f,-\omega_1}\rangle) \tag{10}$$

The first-order response wave functions can be expressed as

$$\langle\Phi_\rho|\mathcal{X}_x^{k,\omega}\rangle = \sum_n \langle\Phi_\rho|\mathcal{R}^n\rangle \frac{\langle\mathcal{L}^n|\hat{\bar{\mu}}_x|\mathcal{R}^k\rangle}{\mathcal{E}_n - \mathcal{E}_k - \omega} \tag{11}$$

In practice, they are computed by solving the following system of linear equations:

$$\sum_\rho \langle\Phi_\nu|(\hat{\bar{\mathcal{H}}} - \mathcal{E}_k - \omega)|\Phi_\rho\rangle\langle\Phi_\rho|\mathcal{X}_x^{k,\omega}\rangle = \langle\Phi_\nu|\hat{\bar{\mu}}_x|\mathcal{R}^k\rangle \tag{12}$$

Equations 11 and 12 are related by the EOM-EE-CCSD resolvent ($\mathcal{G}^k(\omega)$) expression

$$\mathcal{G}_{\nu\rho}^k(\omega) = \langle\Phi_\nu|(\hat{\bar{\mathcal{H}}} - \mathcal{E}_k - \omega)^{-1}|\Phi_\rho\rangle = \sum_n \frac{\langle\Phi_\nu|\mathcal{R}^n\rangle\langle\mathcal{L}^n|\Phi_\rho\rangle}{\mathcal{E}_n - \mathcal{E}_k - \omega} \tag{13}$$

For EOM-EE-CCSD, Φ_ν and Φ_ρ in eqs 11−13 span the reference, singly excited, and doubly excited determinant spaces; terms with higher excited determinants do not survive.

Once the 2PA moments are computed, the 2PA strength tensor is constructed according to

$$S_{wx,yz}^{gf}(\omega_1, \omega_2) = \frac{1}{2}(M_{wx}^{g\leftarrow f}(-\omega_1, -\omega_2))(M_{yz}^{f\leftarrow g}(\omega_1, \omega_2)) + \frac{1}{2}(M_{yz}^{g\leftarrow f}(-\omega_1, -\omega_2))^*(M_{wx}^{f\leftarrow g}(\omega_1, \omega_2))^* \tag{14}$$

where "$*$" denotes complex conjugation. The 2PA strength tensor elements are then used for computing the microscopic 2PA cross section δ^{2PA} (in atomic units (au)) as follows:

$$\delta^{\mathrm{2PA}}(\omega_1, \omega_2) = \frac{F}{30}\sum_{x,y} S_{xx,yy}(\omega_1, \omega_2) + \frac{G}{30}\sum_{x,y} S_{xy,xy}(\omega_1, \omega_2) + \frac{H}{30}\sum_{x,y} S_{xy,yx}(\omega_1, \omega_2) \tag{15}$$

with $F = G = H = 2$ for parallel linearly polarized light. For degenerate photons of frequency ω, δ^{2PA} is then converted to the macroscopic 2PA cross section σ^{2PA} in GMs according to

$$\sigma^{\mathrm{2PA}}(\omega) = \frac{4\pi^2\alpha {a_0}^5\omega^2}{c\Gamma}(\delta^{\mathrm{2PA}}(\omega)) \tag{16}$$

where c is the speed of light, a_0 is the Bohr radius, α is the fine-structure constant, and Γ is the phenomenological lifetime broadening.

2.3. Dealing with the Continuum in the Response Domain. For ω in the X-ray regime, computing first-order response wave functions within standard EOM-CC (eq 12) often results in erratic behavior of solvers.[11−13] One reason for this is similar to the case of computing core-level states with standard EOM-CC. Since the response wave functions can be expressed as a linear combination of all states of the system (eq 11) and the contribution of high-lying states to the response states is often dominant due to the near-resonance condition, the coupling of these response states to the valence continuum is significant and leads to divergences.

This coupling can be omitted by using the CVS Hamiltonian $\hat{\bar{H}}$, which is block diagonal in the core-excited and valence-excited determinant spaces. However, simply using $\hat{\bar{H}}$ instead of $\hat{\bar{\mathcal{H}}}$ for computing response wave functions in eq 12 is not sufficient for fixing the erratic behavior of the solvers. The X-ray response wave functions can include non-negligible contributions (coming from $\hat{\bar{H}}^{\mathrm{val}}$) from high-lying valence resonances, which can also decay via the coupling to the valence doubly excited determinants; this coupling contributes to the erratic behavior of the valence doubly excited determinants in the course of the iterative procedure. In addition, the diagonal preconditioner associated with the doubles−doubles block of $\hat{\bar{H}}^{\mathrm{val}}$ is no longer a good approximation to it in the X-ray energy range, crippling the convergence. As noted in refs 11, 12, and 13, lower-level theories such as TD-DFT, CIS (configuration interaction singles), CC2, and ADC(2) either do not have doubly excited determinants (which are primarily responsible for the erratic behavior of solvers) or include them in a perturbative fashion with a diagonal doubles−doubles block (the preconditioner is exact). Therefore, the decay channels are

https://doi.org/10.1021/acs.jctc.2c00541
J. Chem. Theory Comput. 2022, 18, 6189−6202

blocked and the response equations typically converge without a problem.

References 11, 12, and 13 introduced the CVS-0 approach, which simply substitutes $\hat{\bar{\mathcal{H}}}$ with the CVS-0 Hamiltonian ($\hat{\bar{H}}^{\text{core}}$) in eq 12. Thus, the X-ray response wave functions are computed within the configuration space of core-excited determinants only, leading to convergent solutions. Note that, in contrast to ref 13, refs 11 and 12 use a different nomenclature and refer to $\hat{\bar{H}}^{\text{core}}$ as the CVS-CC-RSP and fc-CVS-EOM-CC Hamiltonian, respectively. The use of the CVS-0 Hamiltonian effectively replaces the sum over all states in the EOM-CC expectation-value approach for computing 2P moments with a sum over just the core-excited states; the contribution of valence-excited states to the SOS moments is omitted. This is justified for most RIXS transitions for which the dominant contribution to the moments arises from nearly resonant core-excited states.[36]

In contrast to RIXS, in X2PA, the core-excitation energies can be significantly different from the energies of the two absorbed photons. Then, it is reasonable to assume that the near-resonance contribution can arise from not only the core-excited states but also from low-lying and high-lying valence states. For such cases, the CVS-0 approach would miss important contributions to the X2PA moments; therefore, approaches that can include the valence contribution are desirable.

To recover the valence contribution to the SOS moments without spoiling the convergence of X-ray response solutions, ref 13 introduced a hierarchy of approximations in which the fc-CVS-EOM-CCSD resolvent $\mathcal{G}^k(\omega)$ was approximated as a sum of a core fc-CVS-EOM-CCSD resolvent $G^{\text{core},k}(\omega)$ and a valence resolvent $F^{\text{val},k}(\omega)$ that approximates the valence fc-CVS-EOM-CCSD resolvent $G^{\text{val},k}(\omega)$, where

$$G^{\text{core},k}_{\nu\rho}(\omega) = \langle \Phi_\nu | (\hat{\bar{H}}^{\text{core}} - E_k - \omega)^{-1} | \Phi_\rho \rangle \tag{17}$$

and

$$G^{\text{val},k}_{\nu\rho}(\omega) = \langle \Phi_\nu | (\hat{\bar{H}}^{\text{val}} - E_k - \omega)^{-1} | \Phi_\rho \rangle \tag{18}$$

where E_k is the energy of the k^{th} eigenstate of the fc-CVS-EOM-CCSD Hamiltonian. The approximate valence resolvent can, for example, originate from lower-level methods (e.g., valence fc-CVS-EOM-CCS, valence fc-CVS-EOM-CC2, etc.) for which the valence response is restricted to the valence singly excited determinant space and the doubly excited determinants are either omitted or included in a perturbative fashion in the response equations. An alternative approach involves approximating the $\hat{\bar{H}}^{\text{val}}$ block of the fc-CVS-EOM-CCSD Hamiltonian by its valence singles−singles block, omitting the problematic coupling of the valence singly and doubly excited determinants and the preconditioning of valence doubles−doubles block in the X-ray regime. When the CVS-0 approach is augmented by this latter approximate valence resolvent $F^{\text{uS},k}(\omega)$, the approach is referred to as the CVS-uS ("uS" stands for "uncoupled valence singles") approach. In effect, such approaches only approximate the intermediate states in the SOS expressions of two-photon moments while still using the high-level correlated energies and wave functions of the initial and final states. Further, since the intermediate states in the SOS expressions dominated by doubly excited valence determinants do not couple significantly with the ground state via the one-electron dipole moment operator, the impact of the omission (or perturbative inclusion) of valence doubly excited determinants is primarily through the dilution of dynamical correlation in the energies and wave functions of the intermediate states involved in the valence resolvent.

Since the computed multiphoton properties such as 2PA cross sections can be strongly sensitive to the level of electronic correlation,[60] independent approximations to the valence and core resolvents in our cherry-picking approach may lead to an unbalanced treatment of the core and valence contributions to the X2PA spectra. Therefore, different approximations of the valence resolvent (fc-CVS-EOM-CCS, fc-CVS-EOM-CC2, CVS-uS) may yield different X2PA spectra; similar differences were noted in ref 13 in the context of RIXS. Here, we focus on the CVS-uS approach and leave the search for the most balanced approximation for modeling X2PA spectra for future studies as it will require comparisons with experiments. On the basis of a configurational analysis of 2PA channels in section 2.5, we expect the CVS-uS approximation to give a fairly balanced description of the valence and core contributions to the X2PA spectra for the benchmark systems studied here.

2.4. 2PA Moments within the CVS-uS Approach. Within the CVS-uS approach, the EOM-EE-CCSD-parameterized sum over states for the 2PA moments is a combination of a sum over valence-excited "uS" states plus the contribution from the CCSD state as an intermediate and a sum over core-excited states as follows:

$$\begin{aligned} M^{f\leftarrow g}_{xy}(\omega_1, \omega_2) = & -\frac{\langle L^f|\hat{\tilde{\mu}}_y|R^0\rangle\langle L^0|\hat{\tilde{\mu}}_x|R^g\rangle}{E_0 - E_g - \omega_1} - \frac{\langle L^f|\hat{\tilde{\mu}}_x|R^0\rangle\langle L^0|\hat{\tilde{\mu}}_y|R^g\rangle}{E_0 - E_g - \omega_2} \\ & - \sum_{n\neq 0}^{\text{uS}} \left(\frac{\langle L^f|\hat{\tilde{\mu}}_y|\tilde{R}^n\rangle\langle \tilde{L}^n|\hat{\tilde{\mu}}_x|R^g\rangle}{\tilde{E}_n - E_g - \omega_1} + \frac{\langle L^f|\hat{\tilde{\mu}}_x|\tilde{R}^n\rangle\langle \tilde{L}^n|\hat{\tilde{\mu}}_y|R^g\rangle}{\tilde{E}_n - E_g - \omega_2} \right) \\ & - \sum_{n}^{\text{core}} \left(\frac{\langle L^f|\hat{\tilde{\mu}}_y|R^n\rangle\langle L^n|\hat{\tilde{\mu}}_x|R^g\rangle}{E_n - E_g - \omega_1} + \frac{\langle L^f|\hat{\tilde{\mu}}_x|R^n\rangle\langle L^n|\hat{\tilde{\mu}}_y|R^g\rangle}{E_n - E_g - \omega_2} \right) \end{aligned} \tag{19}$$

and

$$\begin{aligned} M^{g\leftarrow f}_{xy}(-\omega_1, -\omega_2) = & -\frac{\langle L^g|\hat{\tilde{\mu}}_x|R^0\rangle\langle L^0|\hat{\tilde{\mu}}_y|R^f\rangle}{E_0 - E_f + \omega_2} - \frac{\langle L^g|\hat{\tilde{\mu}}_y|R^0\rangle\langle L^0|\hat{\tilde{\mu}}_x|R^f\rangle}{E_0 - E_f + \omega_1} \\ & - \sum_{n\neq 0}^{\text{uS}} \left(\frac{\langle L^g|\hat{\tilde{\mu}}_x|\tilde{R}^n\rangle\langle \tilde{L}^n|\hat{\tilde{\mu}}_y|R^f\rangle}{\tilde{E}_n - E_f + \omega_2} + \frac{\langle L^g|\hat{\tilde{\mu}}_y|\tilde{R}^n\rangle\langle \tilde{L}^n|\hat{\tilde{\mu}}_x|R^f\rangle}{\tilde{E}_n - E_f + \omega_1} \right) \\ & - \sum_{n}^{\text{core}} \left(\frac{\langle L^g|\hat{\tilde{\mu}}_x|R^n\rangle\langle L^n|\hat{\tilde{\mu}}_y|R^f\rangle}{E_n - E_f + \omega_2} + \frac{\langle L^g|\hat{\tilde{\mu}}_y|R^n\rangle\langle L^n|\hat{\tilde{\mu}}_x|R^f\rangle}{E_n - E_f + \omega_1} \right) \end{aligned} \tag{20}$$

Here, $\langle L^0|$ and $|R^0\rangle$ correspond to the CCSD state; note that often, for X2PA, the CCSD state is the initial state g. $\tilde{E}_n$ and $\langle \tilde{L}^n|$ and $|\tilde{R}^n\rangle$ are the n^{th} eigenenergy and left and right eigenvectors, respectively, that diagonalize the $\hat{\bar{H}}^{\text{uS}}$ block, which is defined as the $\hat{\bar{H}}^{\text{val}}$ block with singles−doubles, doubles−singles, and doubles−doubles blocks zeroed out and the CCSD state projected out. These sums in eqs 19 and 20 are separately recast into closed-form expressions using response wave functions that span separate determinant spaces as follows:

https://doi.org/10.1021/acs.jctc.2c00541
J. Chem. Theory Comput. 2022, 18, 6189−6202

$$M_{xy}^{f\leftarrow g}(\omega_1, \omega_2) = -\frac{\langle L^f|\hat{\bar{\mu}}_y|R^0\rangle\langle L^0|\hat{\bar{\mu}}_x|R^g\rangle}{E_0 - E_g - \omega_1} - \frac{\langle L^f|\hat{\bar{\mu}}_x|R^0\rangle\langle L^0|\hat{\bar{\mu}}_y|R^g\rangle}{E_0 - E_g - \omega_2} - \langle L^f|\hat{\bar{\mu}}_y|X_x^{\mathrm{uS},g,\omega_1}\rangle - \langle L^f|\hat{\bar{\mu}}_x|X_y^{\mathrm{uS},g,\omega_2}\rangle - \langle L^f|\hat{\bar{\mu}}_y|X_x^{\mathrm{core},g,\omega_1}\rangle - \langle L^f|\hat{\bar{\mu}}_x|X_y^{\mathrm{core},g,\omega_2}\rangle \quad (21)$$

and

$$M_{xy}^{g\leftarrow f}(-\omega_1, -\omega_2) = -\frac{\langle L^g|\hat{\bar{\mu}}_x|R^0\rangle\langle L^0|\hat{\bar{\mu}}_y|R^f\rangle}{E_0 - E_f + \omega_2} - \frac{\langle L^g|\hat{\bar{\mu}}_y|R^0\rangle\langle L^0|\hat{\bar{\mu}}_x|R^f\rangle}{E_0 - E_f + \omega_1} - \langle L^g|\hat{\bar{\mu}}_x|X_y^{\mathrm{uS},f,-\omega_2}\rangle - \langle L^g|\hat{\bar{\mu}}_y|X_x^{\mathrm{uS},f,-\omega_1}\rangle - \langle L^g|\hat{\bar{\mu}}_x|X_y^{\mathrm{core},f,-\omega_2}\rangle - \langle L^g|\hat{\bar{\mu}}_y|X_x^{\mathrm{core},f,-\omega_1}\rangle \quad (22)$$

The CVS-uS response equations are given by

$$\sum_\rho \langle\Phi_\nu|(\hat{\bar{H}}^{\mathrm{uS}} - E_k - \omega)|\Phi_\rho\rangle\langle\Phi_\rho|X_x^{\mathrm{uS},k,\omega}\rangle = \langle\Phi_\nu|\hat{\bar{\mu}}_x|R^k\rangle - \langle\Phi_\nu|R^0\rangle\langle L^0|\hat{\bar{\mu}}_x|R^k\rangle; \quad \Phi_\nu, \Phi_\rho \in \{\Phi_0, \Phi_i^a\} \quad (23)$$

and

$$\sum_\rho \langle\Phi_\nu|(\hat{\bar{H}}^{\mathrm{core}} - E_k - \omega)|\Phi_\rho\rangle\langle\Phi_\rho|X_x^{\mathrm{core},k,\omega}\rangle = \langle\Phi_\nu|\hat{\bar{\mu}}_x|R^k\rangle; \quad \Phi_\nu, \Phi_\rho \in \{\Phi_I^a, \Phi_{Ij}^{ab}, \Phi_{IJ}^{ab}\} \quad (24)$$

Here, i, j, ... represent the valence occupied orbitals; I, J, ... represent the core occupied orbitals; and a, b, ... represent the unoccupied orbitals. The state index k in $|R^k\rangle$ refers to either the ground state g or the final state f. Note that we have projected out the CCSD state in the right-hand side of eq 23 to account for its omission in the sum over valence "uS" states in eqs 19 and 20.

2.5. Configurational Analysis of 2PA Channels. To better understand the CVS-uS approximation to the fc-CVS-EOM-EE-CCSD resolvent for computing X2PA moments and to provide a rationale for it, here, we analyze contributions to the 2PA moments in terms of leading electronic configurations. Tables 1 and 2 present the configurational channel analysis of the X2PA moments between an initial (EOM-EE-)CCSD state with frozen core and a final fc-CVS-EOM-EE-CCSD wave function. We define these 2PA configurational channels as the 2PA coupling terms between Slater determinants involved in the wave functions of the initial and final states through the Slater determinants involved in the intermediate wave function. Here, we neglect dynamical correlation effects arising from the cluster operator $\hat{T}$. Our aim is to understand which 2PA channels are fully captured, approximated, or not captured by the CVS-uS approximation to the fc-CVS-EOM-EE-CCSD resolvent. In addition, the channel analysis can help us better understand the impact of different types of bound and continuum intermediate states on the 2PA moments.

First, we consider only the dominant electronic configuration in the initial wave function such that $\Psi^g \sim \Phi_0$ for the CCSD state and $\Psi^f \sim \Phi_J^b$ for the core-excited final state. Within this simplified model, there are just four 2PA channels that need to be considered: channels (1), (2), (21), and (22) in Tables 1 and 2. Channels (1) and (2) are captured exactly by the CVS-0 resolvent, relative to the fc-CVS-EOM-EE-CCSD resolvent, and dominate the contributions of core-excited pre-edge states that lie below the respective core-ionization energy. These channels can also show resonance enhancement when one of the two absorbed photons is in the infrared/UV−vis regime and the other is an X-ray photon that is nearly resonant with a core-excited state. Similarly, channels (21) and (22), which are only approximated by the uS resolvent, relative to the fc-CVS-EOM-EE-CCSD resolvent, can show resonance enhancement when the infrared/UV−vis photon is nearly resonant with a valence-excited state.

Next, if we include other core-excited determinants in the final wave function, the CVS-uS approximation captures all channels involving Φ_0 (channels (1)−(4) and channels (21)−(23) in Tables 1 and 2). Significantly, the couplings of Φ_0 with the dominant singly core-excited configurations (CV) of the final wave function involve only the singly excited valence or core excited determinants as intermediates, which are captured in the CVS-uS approach.

CVS-uS, however, does not capture all the channels involving the dominant configuration when $\Psi^g \sim \Phi_i^a$ is an EOM-EE-CCSD state (channels (30) and (31)). Unless enhanced by near-resonance consideration, these channels only give small contributions due to the small coefficients of the nondominant COVV configurations in Ψ^f with which the dominant OV configurations in Ψ^g couple. Further, when ω is an X-ray frequency, the near-resonance conditions in these channels in Table 1 ($\epsilon_b - \epsilon_l \approx \omega$ and $\epsilon_c - \epsilon_k \approx \omega$ in channels (30) and (31), respectively) imply that the unoccupied orbitals b and c are high-lying and highly oscillatory, resulting in negligible couplings in the numerators of these channels. Similarly, for these missed channels in Table 2, near-resonance conditions ($\epsilon_l - \epsilon_J \approx \omega$) are rare due to the sparsity of occupied and core orbitals in typical molecular systems; therefore, these channels do not contribute significantly in general.

Next, we analyze the couplings of different types of valence and core states with the initial and final states involved in the X2PA process within the uncorrelated picture. The valence doubly excited determinants do not couple with the reference and CV determinants through the dipole moment operator. Within the fc-CVS-EOM-EE-CCSD framework, the final states are predominantly singly excited with leading CV configurations involving low-lying unoccupied orbitals. These states do not couple through the dipole moment operator with the leading OV configurations in valence shape resonances in which the unoccupied orbitals are high-lying continuum orbitals. On the other hand, the leading OV configurations of valence Feshbach resonances can couple to these leading CV configurations in the final states through the one-electron operator (channels (22), (24), and (28)). The 2PA channels corresponding to these couplings are captured in the CVS-uS approach. Only the couplings between the nondominant COVV configurations in the final wave function and OOVV configurations in the intermediate wave functions are omitted through the omitted 2PA channels (30)−(33), which can only be significant through resonance enhancement.

3. COMPUTATIONAL DETAILS

The CVS-0 and CVS-uS resolvent approaches for X2PA cross sections within the (fc-CVS-)EOM-EE-CCSD framework are implemented in a development version of the Q-Chem

https://doi.org/10.1021/acs.jctc.2c00541
J. Chem. Theory Comput. 2022, 18, 6189−6202

Table 1. Configurational Analysis of the Leading Channels in X2PA Moment, $M^{f\leftarrow g}$, Where $\Psi^g = r_0\Phi_0 + \sum_{ia} r_i^a\Phi_i^a + (1/4)\sum_{ijab} r_{ij}^{ab}\Phi_{ij}^{ab}$ Is the Wave Function of the Initial State g and $\Psi^f = \sum_{Ia} l_I^a\Phi_I^a + (1/2)\sum_{Ijab} l_{Ij}^{ab}\Phi_{Ij}^{ab} + (1/4)\sum_{IJab} l_{IJ}^{ab}\Phi_{IJ}^{ab}$ Is the Wave Function of the Final State f[a]

(i) Channels captured by CVS−0

$$\frac{\langle\Phi_J^b\mid\mu\mid\Phi_I^b\rangle\langle\Phi_I^b\mid\mu\mid\Phi_0\rangle}{\epsilon_b-\epsilon_I-\omega}\ (1) \qquad \frac{\langle\Phi_J^b\mid\mu\mid\Phi_J^a\rangle\langle\Phi_J^a\mid\mu\mid\Phi_0\rangle}{\epsilon_a-\epsilon_J-\omega}\ (2) \qquad \frac{\langle\Phi_{JK}^{bc}\mid\mu\mid\Phi_J^b\rangle\langle\Phi_J^b\mid\mu\mid\Phi_0\rangle}{\epsilon_b-\epsilon_J-\omega}\ (3) \qquad \frac{\langle\Phi_{Jk}^{bc}\mid\mu\mid\Phi_J^b\rangle\langle\Phi_J^b\mid\mu\mid\Phi_0\rangle}{\epsilon_b-\epsilon_J-\omega}\ (4)$$

$$\frac{\langle\Phi_J^b\mid\mu\mid\Phi_{Ji}^{ba}\rangle\langle\Phi_{Ji}^{ba}\mid\mu\mid\Phi_i^a\rangle}{\epsilon_b-\epsilon_J-\omega}\ (5) \qquad \frac{\langle\Phi_J^b\mid\mu\mid\Phi_{Ji}^{ba}\rangle\langle\Phi_{Ji}^{ba}\mid\mu\mid\Phi_i^b\rangle}{\epsilon_a-\epsilon_J-\omega}\ (6) \qquad \frac{\langle\Phi_J^b\mid\mu\mid\Phi_I^b\rangle\langle\Phi_I^b\mid\mu\mid\Phi_i^b\rangle}{\epsilon_i-\epsilon_I-\omega}\ (7) \qquad \frac{\langle\Phi_J^b\mid\mu\mid\Phi_J^a\rangle\langle\Phi_J^a\mid\mu\mid\Phi_i^a\rangle}{\epsilon_i-\epsilon_J-\omega}\ (8)$$

$$\frac{\langle\Phi_{Jk}^{bc}\mid\mu\mid\Phi_J^b\rangle\langle\Phi_J^b\mid\mu\mid\Phi_i^b\rangle}{\epsilon_i-\epsilon_J-\omega}\ (9) \qquad \frac{\langle\Phi_{JK}^{cb}\mid\mu\mid\Phi_{Ji}^{cb}\rangle\langle\Phi_{Ji}^{cb}\mid\mu\mid\Phi_i^b\rangle}{\epsilon_c-\epsilon_J-\omega}\ (10) \qquad \frac{\langle\Phi_{Jk}^{bc}\mid\mu\mid\Phi_J^b\rangle\langle\Phi_J^b\mid\mu\mid\Phi_i^b\rangle}{\epsilon_i-\epsilon_J-\omega}\ (11) \qquad \frac{\langle\Phi_{Jk}^{bc}\mid\mu\mid\Phi_{Jl}^{bc}\rangle\langle\Phi_{Jl}^{bc}\mid\mu\mid\Phi_l^c\rangle}{\epsilon_b-\epsilon_J-\omega}\ (12)$$

$$\frac{\langle\Phi_{Jk}^{bc}\mid\mu\mid\Phi_{Lk}^{bc}\rangle\langle\Phi_{Lk}^{bc}\mid\mu\mid\Phi_k^c\rangle}{\epsilon_b-\epsilon_L-\omega}\ (13) \qquad \frac{\langle\Phi_{Jk}^{bc}\mid\mu\mid\Phi_{Jk}^{bd}\rangle\langle\Phi_{Jk}^{bd}\mid\mu\mid\Phi_k^d\rangle}{\epsilon_b-\epsilon_J-\omega}\ (14) \qquad \frac{\langle\Phi_{Jk}^{bc}\mid\mu\mid\Phi_{Jk}^{bd}\rangle\langle\Phi_{Jk}^{bd}\mid\mu\mid\Phi_k^b\rangle}{\epsilon_d-\epsilon_J-\omega}\ (15) \qquad \frac{\langle\Phi_J^b\mid\mu\mid\Phi_{Jk}^{bc}\rangle\langle\Phi_{Jk}^{bc}\mid\mu\mid\Phi_{lk}^{bc}\rangle}{\epsilon_l-\epsilon_J-\omega}\ (16)$$

$$\frac{\langle\Phi_{JK}^{bc}\mid\mu\mid\Phi_{Jl}^{bc}\rangle\langle\Phi_{Jl}^{bc}\mid\mu\mid\Phi_{il}^{bc}\rangle}{\epsilon_i-\epsilon_J-\omega}\ (17) \qquad \frac{\langle\Phi_{Jl}^{bc}\mid\mu\mid\Phi_{Jl}^{bd}\rangle\langle\Phi_{Jl}^{bd}\mid\mu\mid\Phi_{kl}^{bd}\rangle}{\epsilon_k-\epsilon_J-\omega}\ (18) \qquad \frac{\langle\Phi_{Jl}^{bc}\mid\mu\mid\Phi_{Kl}^{bc}\rangle\langle\Phi_{Kl}^{bc}\mid\mu\mid\Phi_{il}^{bc}\rangle}{\epsilon_i-\epsilon_K-\omega}\ (19) \qquad \frac{\langle\Phi_{Jl}^{bc}\mid\mu\mid\Phi_{Jk}^{bc}\rangle\langle\Phi_{Jk}^{bc}\mid\mu\mid\Phi_{ik}^{bc}\rangle}{\epsilon_i-\epsilon_J-\omega}\ (20)$$

(ii) Channels approximated by uS and the term with the CCSD state as intermediate

$$\frac{\langle\Phi_J^b\mid\mu\mid\Phi_0\rangle\langle\Phi_0\mid\mu\mid\Phi_0\rangle}{-\omega}\ (21) \qquad \frac{\langle\Phi_J^b\mid\mu\mid\Phi_i^b\rangle\langle\Phi_i^b\mid\mu\mid\Phi_0\rangle}{\epsilon_b-\epsilon_i-\omega}\ (22) \qquad \frac{\langle\Phi_{Jk}^{bc}\mid\mu\mid\Phi_k^c\rangle\langle\Phi_k^c\mid\mu\mid\Phi_0\rangle}{\epsilon_c-\epsilon_k-\omega}\ (23) \qquad \frac{\langle\Phi_J^b\mid\mu\mid\Phi_i^b\rangle\langle\Phi_i^b\mid\mu\mid\Phi_i^a\rangle}{\epsilon_b-\epsilon_a-\omega}\ (24)$$

$$\frac{\langle\Phi_J^b\mid\mu\mid\Phi_0\rangle\langle\Phi_0\mid\mu\mid\Phi_i^a\rangle}{\epsilon_i-\epsilon_a-\omega}\ (25) \qquad \frac{\langle\Phi_{Jk}^{bc}\mid\mu\mid\Phi_k^c\rangle\langle\Phi_k^c\mid\mu\mid\Phi_k^a\rangle}{\epsilon_c-\epsilon_a-\omega}\ (26) \qquad \frac{\langle\Phi_{Jk}^{bc}\mid\mu\mid\Phi_k^c\rangle\langle\Phi_k^c\mid\mu\mid\Phi_l^c\rangle}{\epsilon_l-\epsilon_k-\omega}\ (27) \qquad \frac{\langle\Phi_J^b\mid\mu\mid\Phi_i^b\rangle\langle\Phi_i^b\mid\mu\mid\Phi_{ij}^{bc}\rangle}{\epsilon_j-\epsilon_c-\omega}\ (28)$$

$$\frac{\langle\Phi_{Jl}^{bc}\mid\mu\mid\Phi_l^c\rangle\langle\Phi_l^c\mid\mu\mid\Phi_{li}^{cd}\rangle}{\epsilon_i-\epsilon_d-\omega}\ (29)$$

(iii) Channels captured by the term with the CCSD state as intermediate but not by uS

$$\frac{\langle\Phi_{Jk}^{bc}\mid\mu\mid\Phi_{lk}^{bc}\rangle\langle\Phi_{lk}^{bc}\mid\mu\mid\Phi_k^c\rangle}{\epsilon_b-\epsilon_l-\omega}\ (30) \qquad \frac{\langle\Phi_{Jk}^{bc}\mid\mu\mid\Phi_{lk}^{bc}\rangle\langle\Phi_{lk}^{bc}\mid\mu\mid\Phi_l^b\rangle}{\epsilon_c-\epsilon_k-\omega}\ (31) \qquad \frac{\langle\Phi_{Jl}^{bc}\mid\mu\mid\Phi_{kl}^{bc}\rangle\langle\Phi_{kl}^{bc}\mid\mu\mid\Phi_{kl}^{bd}\rangle}{\epsilon_c-\epsilon_d-\omega}\ (32) \qquad \frac{\langle\Phi_{Jl}^{bc}\mid\mu\mid\Phi_{kl}^{bc}\rangle\langle\Phi_{kl}^{bc}\mid\mu\mid\Phi_{il}^{bc}\rangle}{\epsilon_i-\epsilon_k-\omega}\ (33)$$

[a]The coefficients of the Slater determinants are omitted in the table.

electronic structure package.[65] py-CCRSP[84] was used for code debugging and testing.

As application, we considered several small systems, namely NH_3, H_2O, HF, Ne, benzene, and *p*-nitroaniline (*p*NA). Despite the lack of published experimental studies on the X2PA spectra of small molecules, these systems can serve as test cases for various theoretical strategies, which can then be developed further by including more (better) physics for tackling more complex systems such as transition-metal compounds.

We use the following Abelian point groups in our calculations: C_s for NH_3; C_{2v} for H_2O, HF, and *p*NA; and D_{2h} for Ne and benzene. We follow Q-Chem symmetry notation (details can be found in refs 45, 85, and 35) instead of Mulliken symmetry notation.[86] The geometries of HF and H_2O were optimized at the DFT/B3LYP[87,88] level of theory with the t-aug-cc-pVTZ basis set. For NH_3, the CCSD/aug-cc-pVTZ optimized geometry was used. The geometries of benzene and *p*NA were taken from previous studies.[12,13,89] All basis sets and geometries used in this study are provided in the Supporting Information.

Core orbitals were frozen in all calculations as prescribed by the (fc-CVS-)EOM-EE-CCSD framework, except for the N and O *K*-edge calculations for *p*NA wherein the lowest four and two core orbitals were frozen, respectively. The CVS-0 and CVS-uS 2PA cross sections with degenerate photons were computed between the CCSD and core-excited states, with the latter obtained within the fc-CVS-EOM-EE-CCSD framework. We used the d-aug-cc-pVTZ basis set for NH_3, t-aug-cc-pVTZ basis set for H_2O and HF, t-aug-cc-pCVTZ basis set augmented with *s* and *p* Rydberg functions for Ne, uC-6-311(2+,+)G** for benzene, and uC-6-311++G** basis set for *p*NA. For each system, we considered all core-excited states below the respective core-ionization energies, i.e., 10, 22, 24, 32, 65, and

https://doi.org/10.1021/acs.jctc.2c00541
J. Chem. Theory Comput. 2022, 18, 6189−6202

Table 2. Configurational Analysis of the Leading Channels in X2PA Moment, $M^{g\leftarrow f}$, Where $\Psi^g = l_0\Phi_0 + \sum_{ia} l_i^a\Phi_i^a + (1/4)\sum_{ijab} l_{ij}^{ab}\Phi_{ij}^{ab}$ Is the Wave Function of the Initial State g and $\Psi^f = \sum_{Ia} r_I^a\Phi_I^a + (1/2)\sum_{Ijab} r_{Ij}^{ab}\Phi_{Ij}^{ab} + (1/4)\sum_{IJab} r_{IJ}^{ab}\Phi_{IJ}^{ab}$ Is the Wave Function of the Final State f[a]

(i) Channels captured by CVS−0

$\frac{\langle\Phi_0\mid\mu\mid\Phi_I^b\rangle\langle\Phi_I^b\mid\mu\mid\Phi_J^b\rangle}{\epsilon_J-\epsilon_I+\omega}$ (1)	$\frac{\langle\Phi_0\mid\mu\mid\Phi_J^a\rangle\langle\Phi_J^a\mid\mu\mid\Phi_J^b\rangle}{\epsilon_a-\epsilon_b+\omega}$ (2)	$\frac{\langle\Phi_0\mid\mu\mid\Phi_J^b\rangle\langle\Phi_J^b\mid\mu\mid\Phi_{JK}^{bc}\rangle}{\epsilon_K-\epsilon_c+\omega}$ (3)	$\frac{\langle\Phi_0\mid\mu\mid\Phi_J^b\rangle\langle\Phi_J^b\mid\mu\mid\Phi_{Jk}^{bc}\rangle}{\epsilon_k-\epsilon_c+\omega}$ (4)
$\frac{\langle\Phi_i^a\mid\mu\mid\Phi_{Ji}^{ba}\rangle\langle\Phi_{Ji}^{ba}\mid\mu\mid\Phi_J^b\rangle}{\epsilon_a-\epsilon_i+\omega}$ (5)	$\frac{\langle\Phi_i^b\mid\mu\mid\Phi_{Ji}^{ba}\rangle\langle\Phi_{Ji}^{ba}\mid\mu\mid\Phi_J^b\rangle}{\epsilon_a-\epsilon_i+\omega}$ (6)	$\frac{\langle\Phi_i^b\mid\mu\mid\Phi_I^b\rangle\langle\Phi_I^b\mid\mu\mid\Phi_J^b\rangle}{\epsilon_J-\epsilon_I+\omega}$ (7)	$\frac{\langle\Phi_i^a\mid\mu\mid\Phi_J^a\rangle\langle\Phi_J^a\mid\mu\mid\Phi_J^b\rangle}{\epsilon_a-\epsilon_b+\omega}$ (8)
$\frac{\langle\Phi_i^b\mid\mu\mid\Phi_J^b\rangle\langle\Phi_J^b\mid\mu\mid\Phi_{Jk}^{bc}\rangle}{\epsilon_k-\epsilon_c+\omega}$ (9)	$\frac{\langle\Phi_i^b\mid\mu\mid\Phi_{Ji}^{cb}\rangle\langle\Phi_{Ji}^{cb}\mid\mu\mid\Phi_{JK}^{cb}\rangle}{\epsilon_K-\epsilon_i+\omega}$ (10)	$\frac{\langle\Phi_i^b\mid\mu\mid\Phi_J^b\rangle\langle\Phi_J^b\mid\mu\mid\Phi_{Jk}^{bc}\rangle}{\epsilon_k-\epsilon_c+\omega}$ (11)	$\frac{\langle\Phi_l^c\mid\mu\mid\Phi_{Jl}^{bc}\rangle\langle\Phi_{Jl}^{bc}\mid\mu\mid\Phi_{Jk}^{bc}\rangle}{\epsilon_k-\epsilon_l+\omega}$ (12)
$\frac{\langle\Phi_k^c\mid\mu\mid\Phi_{Lk}^{bc}\rangle\langle\Phi_{Lk}^{bc}\mid\mu\mid\Phi_{Jk}^{bc}\rangle}{\epsilon_J-\epsilon_L+\omega}$ (13)	$\frac{\langle\Phi_k^d\mid\mu\mid\Phi_{Jk}^{bd}\rangle\langle\Phi_{Jk}^{bd}\mid\mu\mid\Phi_{Jk}^{bc}\rangle}{\epsilon_d-\epsilon_c+\omega}$ (14)	$\frac{\langle\Phi_k^b\mid\mu\mid\Phi_{Jk}^{bd}\rangle\langle\Phi_{Jk}^{bd}\mid\mu\mid\Phi_{Jk}^{bc}\rangle}{\epsilon_d-\epsilon_c+\omega}$ (15)	$\frac{\langle\Phi_{lk}^{bc}\mid\mu\mid\Phi_{Jk}^{bc}\rangle\langle\Phi_{Jk}^{bc}\mid\mu\mid\Phi_J^b\rangle}{\epsilon_c-\epsilon_K+\omega}$ (16)
$\frac{\langle\Phi_{il}^{bc}\mid\mu\mid\Phi_{Jl}^{bc}\rangle\langle\Phi_{Jl}^{bc}\mid\mu\mid\Phi_{JK}^{bc}\rangle}{\epsilon_K-\epsilon_l+\omega}$ (17)	$\frac{\langle\Phi_{kl}^{bd}\mid\mu\mid\Phi_{Jl}^{bd}\rangle\langle\Phi_{Jl}^{bd}\mid\mu\mid\Phi_{Jl}^{bc}\rangle}{\epsilon_d-\epsilon_c+\omega}$ (18)	$\frac{\langle\Phi_{il}^{bc}\mid\mu\mid\Phi_{Kl}^{bc}\rangle\langle\Phi_{Kl}^{bc}\mid\mu\mid\Phi_{Jl}^{bc}\rangle}{\epsilon_J-\epsilon_K+\omega}$ (19)	$\frac{\langle\Phi_{ik}^{bc}\mid\mu\mid\Phi_{Jk}^{bc}\rangle\langle\Phi_{Jk}^{bc}\mid\mu\mid\Phi_{Jl}^{bc}\rangle}{\epsilon_l-\epsilon_k+\omega}$ (20)

(ii) Channels approximated by uS and the term with the CCSD state as intermediate

$\frac{\langle\Phi_0\mid\mu\mid\Phi_0\rangle\langle\Phi_0\mid\mu\mid\Phi_J^b\rangle}{\epsilon_J-\epsilon_b+\omega}$ (21)	$\frac{\langle\Phi_0\mid\mu\mid\Phi_i^b\rangle\langle\Phi_i^b\mid\mu\mid\Phi_J^b\rangle}{\epsilon_J-\epsilon_i+\omega}$ (22)	$\frac{\langle\Phi_0\mid\mu\mid\Phi_k^c\rangle\langle\Phi_k^c\mid\mu\mid\Phi_{Jk}^{bc}\rangle}{\epsilon_J-\epsilon_b+\omega}$ (23)	$\frac{\langle\Phi_i^a\mid\mu\mid\Phi_i^b\rangle\langle\Phi_i^b\mid\mu\mid\Phi_J^b\rangle}{\epsilon_J-\epsilon_i+\omega}$ (24)
$\frac{\langle\Phi_i^a\mid\mu\mid\Phi_0\rangle\langle\Phi_0\mid\mu\mid\Phi_J^b\rangle}{\epsilon_J-\epsilon_b+\omega}$ (25)	$\frac{\langle\Phi_k^a\mid\mu\mid\Phi_k^c\rangle\langle\Phi_k^c\mid\mu\mid\Phi_{Jk}^{bc}\rangle}{\epsilon_J-\epsilon_b+\omega}$ (26)	$\frac{\langle\Phi_l^c\mid\mu\mid\Phi_k^c\rangle\langle\Phi_k^c\mid\mu\mid\Phi_{Jk}^{bc}\rangle}{\epsilon_J-\epsilon_b+\omega}$ (27)	$\frac{\langle\Phi_{ij}^{bc}\mid\mu\mid\Phi_i^b\rangle\langle\Phi_i^b\mid\mu\mid\Phi_J^b\rangle}{\epsilon_J-\epsilon_i+\omega}$ (28)
$\frac{\langle\Phi_{li}^{cd}\mid\mu\mid\Phi_l^c\rangle\langle\Phi_l^c\mid\mu\mid\Phi_{Jl}^{bc}\rangle}{\epsilon_J-\epsilon_b+\omega}$ (29)			

(iii) Channels captured by the term with the CCSD state as intermediate but not by uS

$\frac{\langle\Phi_k^c\mid\mu\mid\Phi_{lk}^{bc}\rangle\langle\Phi_{lk}^{bc}\mid\mu\mid\Phi_{Jk}^{bc}\rangle}{\epsilon_J-\epsilon_l+\omega}$ (30)	$\frac{\langle\Phi_l^b\mid\mu\mid\Phi_{lk}^{bc}\rangle\langle\Phi_{lk}^{bc}\mid\mu\mid\Phi_{Jk}^{bc}\rangle}{\epsilon_J-\epsilon_l+\omega}$ (31)	$\frac{\langle\Phi_{kl}^{bd}\mid\mu\mid\Phi_{kl}^{bc}\rangle\langle\Phi_{kl}^{bc}\mid\mu\mid\Phi_{Jl}^{bc}\rangle}{\epsilon_J-\epsilon_k+\omega}$ (32)	$\frac{\langle\Phi_{il}^{bc}\mid\mu\mid\Phi_{kl}^{bc}\rangle\langle\Phi_{kl}^{bc}\mid\mu\mid\Phi_{Jl}^{bc}\rangle}{\epsilon_J-\epsilon_k+\omega}$ (33)

[a]The coefficients of the Slater determinants are omitted in the table.

63 states for NH_3, H_2O, HF, Ne, benzene, and *p*NA, respectively. The response equations were solved by using an iterative Davidson-like subspace procedure. All spectra were convoluted by using a Lorentzian broadening function with a half-width at half-maximum of 0.3 eV. In the discussion below, "*X*" labels the ground state and "*c*" is a core-excited state.

4. RESULTS AND DISCUSSION

The bottom panels of Figure 2(a)−(h) compare the experimental and computed XAS spectra of our benchmark systems. The computed XAS spectra are shifted to align with the respective first experimental peak; the shifts are given in the figure legends. These shifts are <1.1 eV and significantly smaller than the corresponding shifts computed at the lower TD-DFT/CAM-B3LYP$_{100\%}$ level of theory in ref 64. The XAS spectra yielded by (fc-CVS-)EOM-EE-CCSD show only small discrepancies with respect to experimental spectra in terms of peak positions and intensities of dominant peaks, compared to similar discrepancies with the TD-DFT approach in ref 64, further highlighting its robustness relative to TD-DFT in modeling XAS. Below, all computed energy values are shifted values. The nonshifted peak positions are reported in the Supporting Information.

The top two panels in Figure 2(a)−(h) provide the X2PA spectra computed, respectively, with the CVS-0 and CVS-uS resolvents within the (fc-CVS-)EOM-EE-CCSD framework for the benchmark systems (shifted similar to XAS). We note that the CVS-0 results are not to be construed as an approximation to the CVS-uS results; rather, the CVS-0 data provide separate estimates of the core and valence contributions to the X2PA

https://doi.org/10.1021/acs.jctc.2c00541
J. Chem. Theory Comput. 2022, 18, 6189−6202

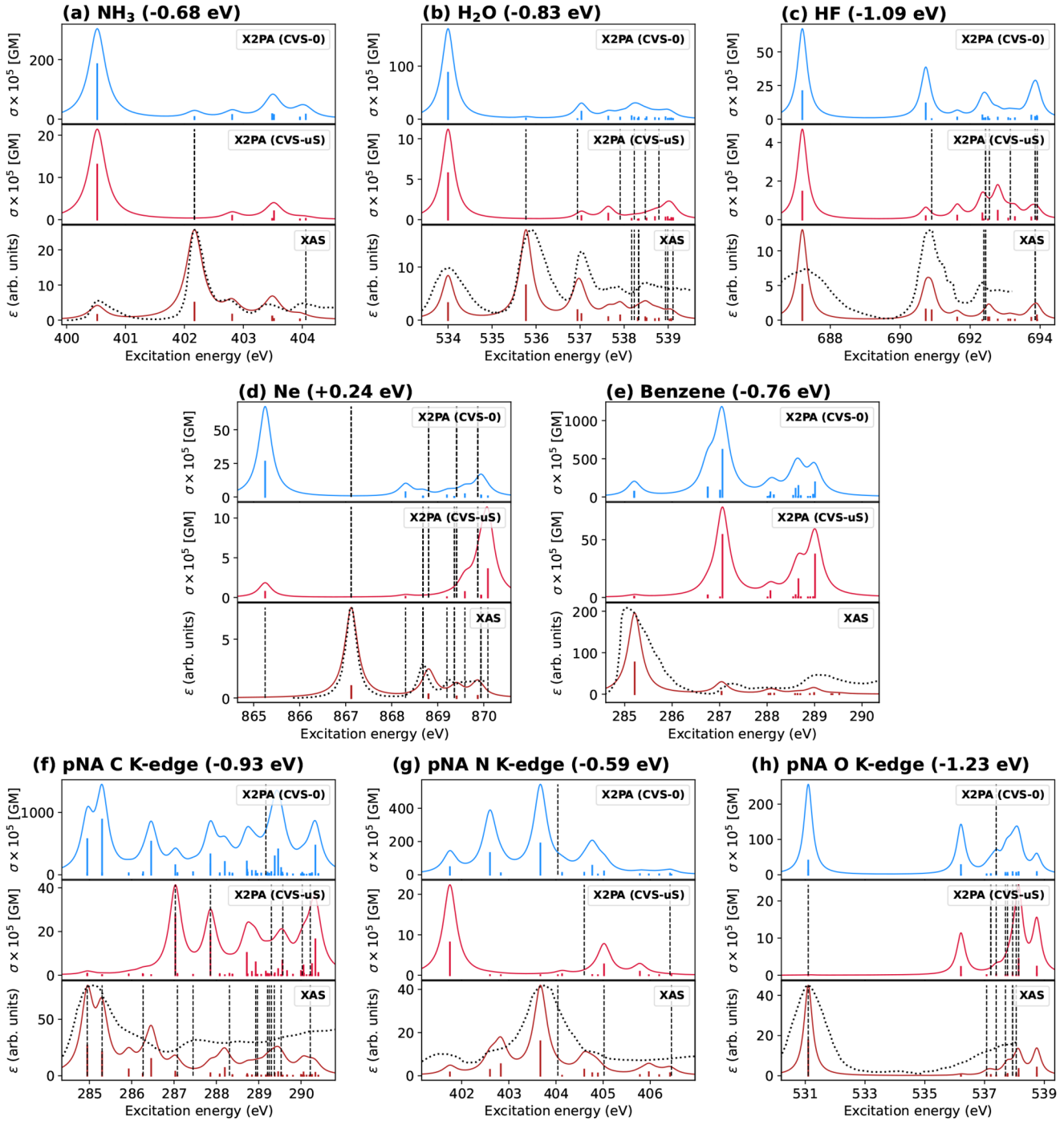

Figure 2. fc-CVS-EOM-EE-CCSD with the d-aug-cc-pVTZ (NH_3), t-aug-cc-pCVTZ (H_2O, HF), t-aug-cc-pCVTZ+Rydberg (Ne), uC-6-311(2+,+)G** (benzene), and uC-6-311++G** (*p*NA) basis sets. XAS and (CVS-0 and CVS-uS) X2PA spectra of (a) NH_3, (b) H_2O, (c) HF, (d) Ne, (e) benzene, (f) *p*NA (C *K*-edge), (g) *p*NA (N *K*-edge), and (h) *p*NA (O *K*-edge). Experimental spectra from ref 90 (NH_3 and H_2O), ref 91 (HF), ref 92 (benzene), ref 93 (Ne), and ref 94 (*p*NA). Black vertical lines correspond to excited states that are dark in the given spectrum. Dark states are omitted from the benzene spectra.

cross sections. Compared to CVS-0, the intensities of the spectra computed with CVS-uS are one order of magnitude smaller across all systems. This is a consequence of cancellation of contributions from the valence states as intermediates and the core states as intermediates. Further, the shapes of these spectra with the two approaches show significant differences. We also note that the magnitudes of the X2PA cross sections ($\sim 10^{-6}$) in atomic units (au) are orders of magnitude smaller than typical valence 2PA cross sections for these systems, a consequence of small overlaps of core orbitals with unoccupied orbitals. However, the X2PA moments used for computing the cross sections are greater than the precision thresholds set in our calculations and, therefore, these moments are numerically reliable.

Response equations for all systems converge within our CVS-0 and CVS-uS setups. Whereas the convergence is, in general,

https://doi.org/10.1021/acs.jctc.2c00541
J. Chem. Theory Comput. 2022, 18, 6189−6202

quick for most systems, for *p*NA, a few "uS" response equations take ∼80 iterations before convergence—a consequence of the very diffuse basis set used for *p*NA and larger valence contributions in *p*NA compared to other systems.

The XAS spectrum of NH_3, discussed in depth in ref 74, is dominated by the peak at 402.2 eV corresponding to the degenerate $XA' \rightarrow c2A'$ and $XA' \rightarrow c1A''$ transitions, i.e., the $1s \rightarrow 3p$ ($XA_1 \rightarrow cE$) transition, with smaller features around 400.5 eV ($1s \rightarrow 3s$), 402.8 eV, and 403.5 eV. In contrast, both the CVS-0 and CVS-uS X2PA spectra are dominated by the $XA' \rightarrow c1A'$ ($1s \rightarrow 3s$) transition at 400.5 eV. The 2PA cross section for the $XA' \rightarrow c2A'$ transition is, in particular, negligible for the CVS-uS approach. Small features at 402.8 eV and 403.5 eV are also present in the CVS-uS spectrum.

Similar to NH_3, the XAS spectrum for H_2O is richer relative to the X2PA spectra (from both the CVS-0 and CVS-uS approaches) and dominated by the three features around 534.0 eV, 535.7 eV, and 537.0 eV. The first feature results from the $XA_1 \rightarrow c1A_1$ transition, the second results from the $XA_1 \rightarrow c1B_1$ transition, and the third results from $XA_1 \rightarrow c1B_2$ and $XA_1 \rightarrow c2A_1$ transitions; see also refs 74 and 95. The X2PA spectrum for both CVS-0 and CVS-uS has a dominant peak corresponding to the $XA_1 \rightarrow c1A_1$ transition with a tail of small features observed in the high-energy region. The CVS-uS X2PA spectrum is also similar to the X2PA spectrum in ref 64.

The computed XAS spectrum for HF shows two dominant peaks around 687.2 eV and 690.8 eV. The former peak arises from the $XA_1 \rightarrow c1A_1$ transition, while the latter originated from the close-lying $XA_1 \rightarrow c2A_1$ and degenerate $XA_1 \rightarrow c1B_1$ and $XA_1 \rightarrow c1B_2$ transitions. Both CVS-0 and CVS-uS X2PA spectra are dominated by the $XA_1 \rightarrow c1A_1$ transition. However, whereas the CVS-0 spectrum also shows a dominant $XA_1 \rightarrow c2A_1$ peak, this transition is not as important in the CVS-uS spectrum. The CVS-uS spectrum instead features close-lying peaks around 692.4 eV and 692.8 eV, arising from the $XA_1 \rightarrow c4A_1$ and $XA_1 \rightarrow c7A_1$ transitions, respectively. Although the shape of the CVS-uS spectrum resembles the X2PA spectrum in ref 64, the smaller features are slightly blue shifted in the former.

XAS and X2PA spectra for neon are complementary to each other. The XAS spectrum, consisting entirely of Rydberg transitions, is dominated by the $1s \rightarrow 3p$ transition, peaked at 867.1 eV, followed by $1s \rightarrow 4p$, $1s \rightarrow 5p$ and $1s \rightarrow 6p$, as allowed according to dipole selection rules.[74,93,95] Relative to the shifts applied to the XAS spectrum in ref 64, the shifts applied in this study are much smaller. The CVS-0 X2PA spectrum has a dominant $1s \rightarrow 3s$ ($XA_g \rightarrow c1A_g$) feature at 865.3 eV, along with smaller features at 868.3 eV and 869.9 eV; the latter arises from $1s \rightarrow 3d$ transitions. In contrast, the CVS-uS spectrum has a dominant feature at 870.1 eV, arising from the $XA_g \rightarrow c11A_g$ transition, followed by a smaller peak at 869.9 eV corresponding to the $1s \rightarrow 3d$ transition. The CVS-uS spectrum resembles the X2PA spectrum in ref 64, even though the $1s \rightarrow 3d$ transitions, which are indicated as the dominant ones in the case of X2PA spectrum in ref 64, are no longer the most dominant. The difference between the CVS-0 and CVS-uS spectra further highlights the importance of including the valence resolvent for computing X2PA cross sections.

Benzene's XAS, also studied in refs 89 and 12, features a dominant peak at 285.2 eV arising from the $XA_g \rightarrow c2B_{1u}$ transition. Smaller features including the ones at 287.0 eV and 289.0 eV are also present, with the former originating from degenerate $XA_g \rightarrow c1B_{2u}$ and $XA_g \rightarrow c2B_{3u}$ transitions and the latter originating from degenerate $XA_g \rightarrow c9B_{2u}$ and $XA_g \rightarrow c12B_{3u}$ transitions. Benzene is centrosymmetric, and its XAS and X2PA are complementary to each other. Whereas the dominant X2PA peak for both CVS-0 and CVS-uS approaches originates from the same $XA_g \rightarrow c2A_g$ transition at 287.1 eV, the shapes of the two spectra are slightly different for the smaller features. Among the smaller features for CVS-uS, the peak at 289.0 eV arising from the $XA_g \rightarrow c12A_g$ transition is dominant. The complementary XAS and X2PA modeling augmented by the corresponding orbital analysis can, in principle, provide rich information on the electronic structure of this highly symmetric molecule.

*p*NA has a large dipole moment and features numerous charge-transfer valence excitations. The computed C *K*-edge XAS spectrum is comparable with the experimental spectrum in ref 94, although experimental features, except the ones around 285.0 eV and 287.5 eV and the shoulder around 286.0 eV, are not well resolved. The dominant feature around 285.0 eV originates from the $XA_1 \rightarrow c1B_2$ and $XA_1 \rightarrow c2B_2$ transitions, both of $1s_C \rightarrow \pi^*$ character. The former transition is characterized by $b_1 \rightarrow a_2$ and $a_1 \rightarrow b_2$ orbital transitions with the core hole delocalized over the two carbons at the *meta* position relative to the nitro group (see the raw data in Table S7 and NTO analysis in Table S8 in the Supporting Information). The latter transition is characterized by a $b_1 \rightarrow a_2$ orbital transition with the core hole delocalized over the two carbons at the *meta* position relative to the amine group. The next two features, one at ≈285.9 eV and the other at 286.5 eV, arise from the $XA_1 \rightarrow c3B_2$ and $XA_1 \rightarrow c5B_2$ transitions, respectively. The first one is due to $1s \rightarrow \pi^*$ transition from the carbon atom bearing the nitro group. The second, also of $1s \rightarrow \pi^*$ type, is an $a_1 \rightarrow b_2$ transition with the core hole originating primarily from the C atom bearing the amino group, with some delocalization over the two nearest carbons. The computed XAS spectrum has a few other relatively intense features such as $XA_1 \rightarrow c1B_1$ at 287.0 eV, $XA_1 \rightarrow c7B_2$ at 288.2 eV, $XA_1 \rightarrow c13A_1$ at 289.5 eV, $XA_1 \rightarrow c11B_2$ at 289.5 eV, $XA_1 \rightarrow c15B_1$ at 290.1 eV, and $XA_1 \rightarrow c20A_1$ at 290.3 eV. Their character (π^*, σ^*, Rydberg) becomes apparent upon inspecting the NTOs in Table S8.

In the CVS-0 X2PA spectrum, many of these same transitions are important along with $XA_1 \rightarrow c1A_1$ at 287.0 eV, $XA_1 \rightarrow c2A_1$ at 287.9 eV, $XA_1 \rightarrow c5A_1$ at 288.7 eV, $XA_1 \rightarrow c7A_1$ at 288.8 eV, $XA_1 \rightarrow c12A_1$ at 289.4 eV, $XA_1 \rightarrow c2B_1$ at 287.9 eV, and $XA_1 \rightarrow c5B_1$ at 288.7 eV. The CVS-uS spectrum, in contrast, is less rich, with only the $XA_1 \rightarrow c1A_1$, $XA_1 \rightarrow c2A_1$, $XA_1 \rightarrow c5A_1$, $XA_1 \rightarrow c8A_1$ (at 288.9 eV), $XA_1 \rightarrow c14A_1$ (at 289.6 eV), $XA_1 \rightarrow c19A_1$ (at 290.3 eV), $XA_1 \rightarrow c20A_1$, and $XA_1 \rightarrow c15B_1$ transitions dominant. *p*NA, therefore, represents yet another system that features a large valence contribution to the X2PA cross sections, highlighting the importance of including the valence resolvent in our model. The dominant transitions in the CVS-uS spectrum, $XA_1 \rightarrow c1A_1$ and $XA_1 \rightarrow c2A_1$, are characterized by different pairs of $a_1 \rightarrow a_1$ and $b_1 \rightarrow b_1$ orbital transitions, and are of σ^*/Rydberg type. For the former, the core hole is delocalized on the carbons *meta* to the amine group, whereas for the latter, the core hole is predominantly centered on the carbons *meta* to the nitro group. The next most intense peak is due to the $XA_1 \rightarrow c20A_1$ transition, characterized by an $a_1 \rightarrow a_1$ transition with the core hole on the carbon atom connected to the nitro group; see Table S8.

Compared to the C *K*-edge spectra, the N and O *K*-edge XAS and X2PA spectra of *p*NA are not as rich, a direct consequence of fewer N and O atoms. The computed N *K*-edge XAS spectrum, which compares well with the experimental spectrum from ref

https://doi.org/10.1021/acs.jctc.2c00541
J. Chem. Theory Comput. 2022, 18, 6189−6202

94, is dominated by the $XA_1 \rightarrow c2B_2$ ($1s \rightarrow \pi^*$) transition at 403.7 eV, which is also dominant in the CVS-0 spectrum. This transition is characterized by the $a_1 \rightarrow b_2$ orbital transition with the core hole localized on the N atom of the nitro group and a delocalized π^* particle orbital (see the raw data in Table S7 and NTO analysis in Table S8). The second dominant feature in the XAS transition originates from two transitions: $XA_1 \rightarrow c1B_2$ at 402.6 eV and $XA_1 \rightarrow c1B_1$ at 402.8 eV. The former is also quite strong in the CVS-0 spectrum and is characterized by the $a_1 \rightarrow b_2$ orbital transition with the core hole localized on N atom of the amine group and another delocalized π^* particle orbital. In contrast to the XAS and CVS-0 spectra, the CVS-uS spectrum shows different dominant features arising from the $XA_1 \rightarrow c1A_1$ and $XA_1 \rightarrow c4A_1$ transitions at 401.8 eV and 405.0 eV, respectively. Remarkably, in both these transitions, the core hole is localized on the amine group's N atom and the nitro group does not participate in the particle orbital. The core transitions from the N atom in the nitro group are basically quenched in the XTPA CVS-uS spectrum.

The O *K*-edge XAS spectrum of *p*NA is even more featureless than the N *K*-edge XAS spectrum and compares well with the experimental spectrum from ref 94. The XAS spectrum has a dominant feature at 531.1 eV originating from the $XA_1 \rightarrow c1B_2$ transition, characterized by an $a_1 \rightarrow b_2$ orbital transition with a delocalized π^* particle orbital and the core hole delocalized on the two oxygen atoms (see the raw data in Table S11 and NTO analysis in Table S12 in the Supporting Information). This transition, along with the degenerate $XA_1 \rightarrow c1A_2$ transition, is also dominant in the CVS-0 spectrum but quenched in the CVS-uS spectrum. These two transitions have the same characteristic π^* particle orbital, with the hole orbitals different (one is the symmetric and the other the antisymmetric combination of the oxygen 1s orbitals). Similar to the N *K*-edge CVS-uS spectrum, the O *K*-edge CVS-uS spectrum is dominated by fully symmetric transitions. In this case, the dominant transitions are $XA_1 \rightarrow c6A_1$, $XA_1 \rightarrow c7A_1$, and $XA_1 \rightarrow c1A_1$ at 538.1 eV, 538.8 eV, and 536.2 eV, respectively. Whereas the first two transitions feature particle orbitals delocalized on the entire molecule, the third transition features a particle orbital that is largely localized at the nitro end of *p*NA. For details on the NTOs involved in the smaller features, we refer to the tabulated raw data used to construct the spectra shown in Figure 2 and the corresponding NTO analyses in the Supporting Information.

5. CONCLUSIONS

We have presented an approach for computing X2PA spectra within the EOM-EE-CCSD framework. Standard iterative procedures for computing the X-ray response wave functions diverge within the EOM-EE-CCSD framework; in this study, we have extended our frozen-core CVS-based strategy of cherry-picking resolvents, mitigating this issue in the computations of X2PA cross sections. The fc-CVS scheme allows us to fragment the EOM-EE-CCSD resolvent into a direct sum of independent core (called "CVS-0") and valence resolvents; X-ray response wave functions in the core- and valence-excitation spaces can, therefore, be computed separately. The valence resolvent is then approximated using the valence singles−singles block of the fc-CVS-EOM-EE-CCSD Hamiltonian, which is the "uS" approximation. We also provided the configurational analysis of X2PA channels to rationalize the CVS-uS approach and showed that the approach captures the most important channels for the 2PA transitions between the CCSD or singly excited valence-excited states and singly excited core-excited states. The X2PA spectra for small benchmark systems computed with this approach are comparable in shape to those from the CPP-TD-DFT approach in ref 64, yet with smaller discrepancies for the (fc-CVS-uS-)EOM-EE-CCSD framework in the peak positions relative to XAS experiments. We also highlighted the importance of the valence contribution to the X2PA moments by comparing the CVS-0 and CVS-uS spectra.

■ ASSOCIATED CONTENT

Supporting Information

The Supporting Information is available free of charge at https://pubs.acs.org/doi/10.1021/acs.jctc.2c00541.

Tabulated data for transition properties, natural transition orbital (NTO) pairs of relevant core transitions at the C, N, and O *K*-edges of *p*NA, Cartesian coordinates, basis sets (PDF)

■ AUTHOR INFORMATION

Corresponding Authors

Kaushik D. Nanda − *Department of Chemistry, University of Southern California, Los Angeles, California 90089, United States;* orcid.org/0000-0002-3447-6678; Email: kaushikdnanda@gmail.com

Anna I. Krylov − *Department of Chemistry, University of Southern California, Los Angeles, California 90089, United States;* orcid.org/0000-0001-6788-5016; Email: krylov@usc.edu

Sonia Coriani − *DTU Chemistry, Technical University of Denmark, DK-2800 Kongens Lyngby, Denmark;* orcid.org/0000-0002-4487-897X; Email: soco@kemi.dtu.dk

Author

Josefine H. Andersen − *DTU Chemistry, Technical University of Denmark, DK-2800 Kongens Lyngby, Denmark;* orcid.org/0000-0002-0534-7463

Complete contact information is available at: https://pubs.acs.org/10.1021/acs.jctc.2c00541

Author Contributions

[§]J.H.A. and K.D.N. contributed equally.

Notes

The authors declare the following competing financial interest(s): A.I.K. is the president and a part-owner of Q-Chem, Inc.

■ ACKNOWLEDGMENTS

J.H.A. and S.C. acknowledge financial support from the Independent Research Fund Denmark—Natural Sciences, RP2 Grant No. 7014-00258B. The Marie Skłodowska-Curie European Training Network "COSINE-COmputational Spectroscopy In Natural sciences and Engineering", Grant Agreement No. 765739, is also acknowledged. The work at USC was supported by the U.S. National Science Foundation (No. CHE-2154482 to A.I.K.).

■ REFERENCES

(1) Stanton, J. F.; Bartlett, R. J. The equation of motion coupled-cluster method. A systematic biorthogonal approach to molecular excitation energies, transition probabilities, and excited state properties. *J. Chem. Phys.* **1993**, *98*, 7029−7039.

(2) Bartlett, R. J.; Musial, M. Coupled-cluster theory in quantum chemistry. *Rev. Mod. Phys.* **2007**, *79*, 291−352.
(3) Krylov, A. I. Equation-of-motion coupled-cluster methods for open-shell and electronically excited species: The hitchhiker's guide to Fock space. *Annu. Rev. Phys. Chem.* **2008**, *59*, 433−462.
(4) Koch, H.; Jørgensen, P. Coupled cluster response functions. *J. Chem. Phys.* **1990**, *93*, 3333−3344.
(5) Christiansen, O.; Jørgensen, P.; Hättig, C. Response functions from Fourier component variational perturbation theory applied to a time-averaged quasienergy. *Int. J. Quantum Chem.* **1998**, *68*, 1−52.
(6) Helgaker, T.; Coriani, S.; Jørgensen, P.; Kristensen, K.; Olsen, J.; Ruud, K. Recent advances in wave function-based methods of molecular property calculations. *Chem. Rev.* **2012**, *112*, 543−631.
(7) Hättig, C.; Christiansen, O.; Jørgensen, P. Multiphoton transition moments and absorption cross sections in coupled cluster response theory employing variational transition moment functionals. *J. Chem. Phys.* **1998**, *108*, 8331−8354.
(8) Friese, D. H.; Hättig, C.; Ruud, K. Calculation of two-photon absorption strengths with the approximate coupled cluster singles and doubles model CC2 using the resolution-of-identity approximation. *Phys. Chem. Chem. Phys.* **2012**, *14*, 1175−1184.
(9) Nanda, K. D.; Krylov, A. I. Two-photon absorption cross sections within equation-of-motion coupled-cluster formalism using resolution-of-the-identity and Cholesky decomposition representations: Theory, implementation, and benchmarks. *J. Chem. Phys.* **2015**, *142*, 064118.
(10) Faber, R.; Coriani, S. Resonant inelastic X-ray scattering and nonresonant X-ray emission spectra from coupled-cluster (damped) response theory. *J. Chem. Theory Comput.* **2019**, *15*, 520−528.
(11) Faber, R.; Coriani, S. Core−valence-separated coupled-cluster-singles-and-doubles complex-polarization-propagator approach to X-ray spectroscopies. *Phys. Chem. Chem. Phys.* **2020**, *22*, 2642−2647.
(12) Nanda, K. D.; Vidal, M. L.; Faber, R.; Coriani, S.; Krylov, A. I. How to stay out of trouble in RIXS calculations within equation-of-motion coupled-cluster damped response theory? Safe hitchhiking in the excitation manifold by means of core-valence separation. *Phys. Chem. Chem. Phys.* **2020**, *22*, 2629−2641.
(13) Nanda, K. D.; Krylov, A. I. Cherry-picking resolvents: A general strategy for convergent coupled-cluster damped response calculations of core-level spectra. *J. Chem. Phys.* **2020**, *153*, 141104.
(14) Hättig, C.; Christiansen, O.; Koch, H.; Jørgensen, P. Frequency-dependent first hyperpolarizabilities using coupled cluster quadratic response theory. *Chem. Phys. Lett.* **1997**, *269*, 428−434.
(15) Hättig, C.; Christiansen, O.; Jørgensen, P. Frequency-dependent second hyperpolarizabilities using coupled cluster cubic response theory. *Chem. Phys. Lett.* **1998**, *282*, 139−146.
(16) O'Neill, D. P.; Kállay, M.; Gauss, J. Calculation of frequency-dependent hyperpolarizabilities using general coupled-cluster models. *J. Chem. Phys.* **2007**, *127*, 134109.
(17) Nanda, K. D.; Krylov, A. I. The orbital picture of the first dipole hyperpolarizability from many-body response theory. *J. Chem. Phys.* **2021**, *154*, 184109.
(18) Hättig, C.; Christiansen, O.; Coriani, S.; Jørgensen, P. Static and frequency-dependent polarizabilities of excited singlet states using coupled cluster response theory. *J. Chem. Phys.* **1998**, *109*, 9237−9243.
(19) Nanda, K. D.; Krylov, A. I.; Gauss, J. Communication: The pole structure of the dynamical polarizability tensor in equation-of-motion coupled-cluster theory. *J. Chem. Phys.* **2018**, *149*, 141101.
(20) Hättig, C.; Jørgensen, P. Derivation of coupled cluster excited states response functions and multiphoton transition moments between two excited states as derivatives of variational functionals. *J. Chem. Phys.* **1998**, *109*, 9219−9236.
(21) Friese, D. H.; Hättig, C.; Rizzo, A. Origin-independent two-photon circular dichroism calculations in coupled cluster theory. *Phys. Chem. Chem. Phys.* **2016**, *18*, 13683−13692.
(22) Coriani, S.; Jørgensen, P.; Helgaker, T.; Hättig, C. Gauge-origin independent magneto-optical activity within coupled cluster response theory. *J. Chem. Phys.* **2000**, *113*, 3561−3572.
(23) Khani, S. K.; Faber, R.; Santoro, F.; Hättig, C.; Coriani, S. UV absorption and magnetic circular dichroism spectra of purine, adenine, and guanine: A coupled cluster study in vacuo and in aqueous solution. *J. Chem. Theory Comput.* **2019**, *15*, 1242−1254.
(24) Faber, R.; Ghidinelli, S.; Hättig, C.; Coriani, S. Magnetic circular dichroism spectra from resonant and damped coupled cluster response theory. *J. Chem. Phys.* **2020**, *153*, 114105.
(25) Gauss, J.; Kallay, M.; Neese, F. Calculation of electronic g-tensors using coupled cluster theory. *J. Phys. Chem. A* **2009**, *113*, 11541−11549.
(26) Sneskov, K.; Schwabe, T.; Kongsted, J.; Christiansen, O. The polarizable embedding coupled cluster method. *J. Chem. Phys.* **2011**, *134*, 104108.
(27) Krause, K.; Klopper, W. Communication: A simplified coupled-cluster Lagrangian for polarizable embedding. *J. Chem. Phys.* **2016**, *144*, 041101.
(28) Slipchenko, L. V. Solvation of the excited states of chromophores in polarizable environment: Orbital relaxation versus polarization. *J. Phys. Chem. A* **2010**, *114*, 8824−8830.
(29) Nanda, K. D.; Krylov, A. I. The effect of polarizable environment on two-photon absorption cross sections characterized by the equation-of-motion coupled-cluster singles and doubles method combined with the effective fragment potential approach. *J. Chem. Phys.* **2018**, *149*, 164109.
(30) Parravicini, V.; Jagau, T.-C. Embedded equation-of-motion coupled-cluster theory for electronic excitation, ionization, electron attachment, and electronic resonances. *Mol. Phys.* **2021**, *119*, e1943029.
(31) Luzanov, A. V.; Sukhorukov, A. A.; Umanskii, V. E. Application of transition density matrix for analysis of excited states. *Theor. Exp. Chem.* **1976**, *10*, 354−361. Russian original: *Teor. Eksp.Khim.* **1974**, *10*, 456.
(32) Luzanov, A. V.; Pedash, V. F. Interpretation of excited states using charge-transfer number. *Theor. Exp. Chem.* **1980**, *15*, 338−341.
(33) Head-Gordon, M.; Grana, A. M.; Maurice, D.; White, C. A. Analysis of electronic transitions as the difference of electron attachment and detachment densities. *J. Phys. Chem.* **1995**, *99*, 14261−14270.
(34) Martin, R. L. Natural transition orbitals. *J. Phys. Chem. A* **2003**, *118*, 4775−4777.
(35) Nanda, K. D.; Krylov, A. I. Visualizing the contributions of virtual states to two-photon absorption cross-sections by natural transition orbitals of response transition density matrices. *J. Phys. Chem. Lett.* **2017**, *8*, 3256−3265.
(36) Nanda, K. D.; Krylov, A. I. A simple molecular orbital picture of RIXS distilled from many-body damped response theory. *J. Chem. Phys.* **2020**, *152*, 244118.
(37) Plasser, F.; Wormit, M.; Dreuw, A. New tools for the systematic analysis and visualization of electronic excitations. I. Formalism. *J. Chem. Phys.* **2014**, *141*, 024106−13.
(38) Plasser, F.; Bäppler, S. A.; Wormit, M.; Dreuw, A. New tools for the systematic analysis and visualization of electronic excitations. II. Applications. *J. Chem. Phys.* **2014**, *141*, 024107−12.
(39) Mewes, S.; Plasser, F.; Krylov, A.; Dreuw, A. Benchmarking excited-state calculations using exciton properties. *J. Chem. Theory Comput.* **2018**, *14*, 710−725.
(40) Plasser, F.; Krylov, A. I.; Dreuw, A. libwfa: Wavefunction analysis tools for excited and open-shell electronic states. *WIREs: Comput. Mol. Sci.* **2022**, *12*, e1595.
(41) Koch, H.; Kobayashi, R.; Sanchez de Merás, A.; Jørgensen, P. Calculation of size-intensive transition moments from the coupled cluster singles and doubles linear response function. *J. Chem. Phys.* **1994**, *100*, 4393−4400.
(42) Coriani, S.; Pawłowski, F.; Olsen, J.; Jørgensen, P. Molecular response properties in equation of motion coupled cluster theory: A time-dependent perspective. *J. Chem. Phys.* **2016**, *144*, 024102.
(43) Christiansen, O.; Halkier, A.; Koch, H.; Jørgensen, P.; Helgaker, T. Integral-direct coupled cluster calculations of frequency-dependent polarizabilities transition probabilities and excited-state properties. *J. Chem. Phys.* **1998**, *108*, 2801.
(44) Pawłowski, F.; Olsen, J.; Jørgensen, P. Molecular response properties from a Hermitian eigenvalue equation for a time-periodic Hamiltonian. *J. Chem. Phys.* **2015**, *142*, 114109.

https://doi.org/10.1021/acs.jctc.2c00541
J. Chem. Theory Comput. 2022, 18, 6189−6202

(45) Nanda, K. D.; Krylov, A. I. Static polarizabilities for excited states within the spin-conserving and spin-flipping equation-of-motion coupled-cluster singles and doubles formalism: Theory, implementation, and benchmarks. *J. Chem. Phys.* **2016**, *145*, 204116.
(46) Stanton, J. F.; Gauss, J. Many-body methods for excited state potential energy surfaces. II. Analytic second derivatives for excited state energies in the equation-of-motion coupled-cluster method. *J. Chem. Phys.* **1995**, *103*, 8931−8943.
(47) Doumy, G.; Roedig, C.; Son, S.-K.; Blaga, C. I.; DiChiara, A. D.; Santra, R.; Berrah, N.; Bostedt, C.; Bozek, J. D.; Bucksbaum, P. H.; Cryan, J. P.; Fang, L.; Ghimire, S.; Glownia, J. M.; Hoener, M.; Kanter, E. P.; Krässig, B.; Kuebel, M.; Messerschmidt, M.; Paulus, G. G.; Reis, D. A.; Rohringer, N.; Young, L.; Agostini, P.; DiMauro, L. F. Nonlinear atomic response to intense ultrashort X-rays. *Phys. Rev. Lett.* **2011**, *106*, 083002.
(48) Tamasaku, K.; Shigemasa, E.; Inubushi, Y.; Katayama, T.; Sawada, K.; Yumoto, H.; Ohashi, H.; Mimura, H.; Yabashi, M.; Yamauchi, K.; Ishikawa, T. X-ray two-photon absorption competing against single and sequential multiphoton processes. *Nat. Photonics* **2014**, *8*, 313−316.
(49) Ghimire, S.; Fuchs, M.; Hastings, J.; Herrmann, S. C.; Inubushi, Y.; Pines, J.; Shwartz, S.; Yabashi, M.; Reis, D. A. Nonsequential two-photon absorption from the *K*-shell in solid zirconium. *Phys. Rev. A* **2016**, *94*, 043418.
(50) Picón, A.; Lehmann, C. S.; Bostedt, C.; Rudenko, A.; Marinelli, A.; Osipov, T.; Rolles, D.; Berrah, N.; Bomme, C.; Bucher, M.; Doumy, G.; Erk, B.; Ferguson, K. R.; Gorkhover, T.; Ho, P. J.; Kanter, E. P.; Krässig, B.; Krzywinski, J.; Lutman, A. A.; March, A. M.; Moonshiram, D.; Ray, D.; Young, L.; Pratt, S. T.; Southworth, S. H. Hetero-site-specific X-ray pump-probe spectroscopy for femtosecond intramolecular dynamics. *Nat. Commun.* **2016**, *7*, 11652.
(51) Hoszowska, J.; Szlachetko, J.; Dousse, J.-C.; Błachucki, W.; Kayser, Y.; Milne, C.; Pajek, M.; Boutet, S.; Messerschmidt, M.; Williams, G.; Chantler, C. T. X-ray two-photon absorption with high fluence XFEL pulses. *J. Phys.: Conf. Ser.* **2015**, *635*, 102009.
(52) Tamasaku, K.; Shigemasa, E.; Inubushi, Y.; Inoue, I.; Osaka, T.; Katayama, T.; Yabashi, M.; Koide, A.; Yokoyama, T.; Ishikawa, T. Nonlinear spectroscopy with X-ray two-photon absorption in metallic copper. *Phys. Rev. Lett.* **2018**, *121*, 083901.
(53) Rouxel, J.; Kowalewski, M.; Mukamel, S. Diffraction-detected sum frequency generation: Novel ultrafast X-ray probe of molecular dynamics. *J. Phys. Chem. Lett.* **2018**, *9*, 3392−3396.
(54) Bruner, A.; Cavaletto, S. M.; Govind, N.; Mukamel, S. Resonant X-ray sum-frequency-generation spectroscopy of *K*-edges in acetyl fluoride. *J. Chem. Theory Comput.* **2019**, *15*, 6832−6839.
(55) Cavaletto, S. M.; Keefer, D.; Mukamel, S. High temporal and spectral resolution of stimulated X-ray raman signals with stochastic free-electron-laser pulses. *Phys. Rev. X* **2021**, *11*, 011029.
(56) Lam, R.; Raj, S.; Pascal, T.; Pemmaraju, C.; Foglia, L.; Simoncig, A.; Fabris, N.; Miotti, P.; Hull, C.; Rizzuto, A.; Smith, J.; Mincigrucci, R.; Masciovecchio, C.; Gessini, A.; Allaria, E.; De Ninno, G.; Diviacco, B.; Roussel, E.; Spampinati, S.; Penco, G.; Di Mitri, S.; Trovó, M.; Danailov, M.; Christensen, S.; Sokaras, D.; Weng, T.-C.; Coreno, M.; Poletto, L.; Drisdell, W.; Prendergast, D.; Giannessi, L.; Principi, E.; Nordlund, D.; Saykally, R.; Schwartz, C. Soft X-ray second harmonic generation as an interfacial probe. *Phys. Rev. Lett.* **2018**, *120*, 023901.
(57) Shwartz, S.; Fuchs, M.; Hastings, J.; Inubushi, Y.; Ishikawa, T.; Katayama, T.; Reis, D.; Sato, T.; Tono, K.; Yudovich, S.; Harris, S. E.; Yabashi, M. X-ray second harmonic generation. *Phys. Rev. Lett.* **2014**, *112*, 163901.
(58) Olsen, J.; Jørgensen, P. Linear and nonlinear response functions for an exact state and for an MCSCF state. *J. Chem. Phys.* **1985**, *82*, 3235.
(59) Rizzo, A.; Coriani, S.; Ruud, K. Response function theory computational approaches to linear and nonlinear optical spectroscopy. In *Computational Strategies for Spectroscopy*; Barone, V., Ed.; John Wiley & Sons, Inc.: Hoboken, NJ, USA, 2012; pp 77−135.
(60) Paterson, M. J.; Christiansen, O.; Pawłowski, F.; Jørgensen, P.; Hättig, C.; Helgaker, T.; Sałek, P. Benchmarking two-photon absorption with CC3 quadratic response theory, and comparison with density-functional response theory. *J. Chem. Phys.* **2006**, *124*, 054322.
(61) Norman, P. A perspective on non resonant and resonant electronic response theory for time-dependent molecular properties. *Phys. Chem. Chem. Phys.* **2011**, *13*, 20519−20535.
(62) Kristensen, K.; Kauczor, J.; Kjærgaard, T.; Jørgensen, P. Quasienergy formulation of damped response theory. *J. Chem. Phys.* **2009**, *131*, 044112.
(63) Kristensen, K.; Kauczor, J.; Thorvaldsen, A. J.; Jørgensen, P.; Kjærgaard, T.; Rizzo, A. Damped response theory description of two-photon absorption. *J. Chem. Phys.* **2011**, *134*, 214104.
(64) Fahleson, T.; Agren, H.; Norman, P. A polarization propagator for nonlinear X-ray spectroscopies. *J. Phys. Chem. Lett.* **2016**, *7*, 1991−1995.
(65) Epifanovsky, E.; Gilbert, A. T. B.; Feng, X.; Lee, J.; Mao, Y.; Mardirossian, N.; Pokhilko, P.; White, A. F.; Coons, M. P.; Dempwolff, A. L.; Gan, Z.; Hait, D.; Horn, P. R.; Jacobson, L. D.; Kaliman, I.; Kussmann, J.; Lange, A. W.; Lao, K. U.; Levine, D. S.; Liu, J.; McKenzie, S. C.; Morrison, A. F.; Nanda, K. D.; Plasser, F.; Rehn, D. R.; Vidal, M. L.; You, Z.-Q.; Zhu, Y.; Alam, B.; Albrecht, B. J.; Aldossary, A.; Alguire, E.; Andersen, J. H.; Athavale, V.; Barton, D.; Begam, K.; Behn, A.; Bellonzi, N.; Bernard, Y. A.; Berquist, E. J.; Burton, H. G. A.; Carreras, A.; Carter-Fenk, K.; Chakraborty, R.; Chien, A. D.; Closser, K. D.; Cofer-Shabica, V.; Dasgupta, S.; de Wergifosse, M.; Deng, J.; Diedenhofen, M.; Do, H.; Ehlert, S.; Fang, P.-T.; Fatehi, S.; Feng, Q.; Friedhoff, T.; Gayvert, J.; Ge, Q.; Gidofalvi, G.; Goldey, M.; Gomes, J.; González-Espinoza, C. E.; Gulania, S.; Gunina, A. O.; Hanson-Heine, M. W. D.; Harbach, P. H. P.; Hauser, A.; Herbst, M. F.; Hernández Vera, M.; Hodecker, M.; Holden, Z. C.; Houck, S.; Huang, X.; Hui, K.; Huynh, B. C.; Ivanov, M.; Jász, A.; Ji, H.; Jiang, H.; Kaduk, B.; Kähler, S.; Khistyaev, K.; Kim, J.; Kis, G.; Klunzinger, P.; Koczor-Benda, Z.; Koh, J. H.; Kosenkov, D.; Koulias, L.; Kowalczyk, T.; Krauter, C. M.; Kue, K.; Kunitsa, A.; Kus, T.; Ladjánszki, I.; Landau, A.; Lawler, K. V.; Lefrancois, D.; Lehtola, S.; Li, R. R.; Li, Y.-P.; Liang, J.; Liebenthal, M.; Lin, H.-H.; Lin, Y.-S.; Liu, F.; Liu, K.-Y.; Loipersberger, M.; Luenser, A.; Manjanath, A.; Manohar, P.; Mansoor, E.; Manzer, S. F.; Mao, S.-P.; Marenich, A. V.; Markovich, T.; Mason, S.; Maurer, S. A.; McLaughlin, P. F.; Menger, M. F. S. J.; Mewes, J.-M.; Mewes, S. A.; Morgante, P.; Mullinax, J. W.; Oosterbaan, K. J.; Paran, G.; Paul, A. C.; Paul, S. K.; Pavošević, F.; Pei, Z.; Prager, S.; Proynov, E. I.; Rák, Á.; Ramos-Cordoba, E.; Rana, B.; Rask, A. E.; Rettig, A.; Richard, R. M.; Rob, F.; Rossomme, E.; Scheele, T.; Scheurer, M.; Schneider, M.; Sergueev, N.; Sharada, S. M.; Skomorowski, W.; Small, D. W.; Stein, C. J.; Su, Y.-C.; Sundstrom, E. J.; Tao, Z.; Thirman, J.; Tornai, G. J.; Tsuchimochi, T.; Tubman, N. M.; Veccham, S. P.; Vydrov, O.; Wenzel, J.; Witte, J.; Yamada, A.; Yao, K.; Yeganeh, S.; Yost, S. R.; Zech, A.; Zhang, I. Y.; Zhang, X.; Zhang, Y.; Zuev, D.; Aspuru-Guzik, A.; Bell, A. T.; Besley, N. A.; Bravaya, K. B.; Brooks, B. R.; Casanova, D.; Chai, J.-D.; Coriani, S.; Cramer, C. J.; Cserey, G.; DePrince, A. E.; DiStasio, R. A.; Dreuw, A.; Dunietz, B. D.; Furlani, T. R.; Goddard, W. A.; Hammes-Schiffer, S.; Head-Gordon, T.; Hehre, W. J.; Hsu, C.-P.; Jagau, T.-C.; Jung, Y.; Klamt, A.; Kong, J.; Lambrecht, D. S.; Liang, W.; Mayhall, N. J.; McCurdy, C. W.; Neaton, J. B.; Ochsenfeld, C.; Parkhill, J. A.; Peverati, R.; Rassolov, V. A.; Shao, Y.; Slipchenko, L. V.; Stauch, T.; Steele, R. P.; Subotnik, J. E.; Thom, A. J. W.; Tkatchenko, A.; Truhlar, D. G.; Van Voorhis, T.; Wesolowski, T. A.; Whaley, K. B.; Woodcock, H. L.; Zimmerman, P. M.; Faraji, S.; Gill, P. M. W.; Head-Gordon, M.; Herbert, J. M.; Krylov, A. I. Software for the frontiers of quantum chemistry: An overview of developments in the Q-Chem 5 package. *J. Chem. Phys.* **2021**, *155*, 084801.
(66) Jagau, T.-C.; Bravaya, K. B.; Krylov, A. I. Extending quantum chemistry of bound states to electronic resonances. *Annu. Rev. Phys. Chem.* **2017**, *68*, 525−553.
(67) Jagau, T.-C. Theory of electronic resonances: fundamental aspects and recent advances. *Chem. Comm* **2022**, *58*, 5205−5224.
(68) Reinhardt, W. P. Complex coordinates in the theory of atomic and molecular structure and dynamics. *Annu. Rev. Phys. Chem.* **1982**, *33*, 223−255.

https://doi.org/10.1021/acs.jctc.2c00541
J. Chem. Theory Comput. 2022, 18, 6189−6202

(69) Moiseyev, N. Quantum theory of resonances: Calculating energies, widths and cross-sections by complex scaling. *Phys. Rep.* **1998**, *302*, 212−293.
(70) Sadybekov, A.; Krylov, A. I. Coupled-cluster based approach for core-ionized and core-excited states in condensed phase: Theory and application to different protonated forms of aqueous glycine. *J. Chem. Phys.* **2017**, *147*, 014107.
(71) Peng, B.; Lestrange, P. J.; Goings, J. J.; Caricato, M.; Li, X. Energy-specific equation-of-motion coupled-cluster methods for high-energy excited states: Application to *K*-edge X-ray absorption Spectroscopy. *J. Chem. Theory Comput.* **2015**, *11*, 4146−4153.
(72) Cederbaum, L. S.; Domcke, W.; Schirmer, J. Many-body theory of core holes. *Phys. Rev. A: At. Mol. Opt. Phys.* **1980**, *22*, 206−222.
(73) Coriani, S.; Koch, H. Communication: X-ray absorption spectra and core-Ionization potentials within a core-valence separated coupled cluster framework. *J. Chem. Phys.* **2015**, *143*, 181103.
(74) Vidal, M. L.; Feng, X.; Epifanovsky, E.; Krylov, A. I.; Coriani, S. New and efficient equation-of-motion coupled-cluster framework for core-excited and core-ionized states. *J. Chem. Theory Comput.* **2019**, *15*, 3117−3133.
(75) Coriani, S.; Koch, H. Erratum: "Communication: X-ray absorption spectra and core-ionization potentials within a core-valence separated coupled cluster framework" [J. Chem. Phys. 143, 181103 (2015)]. *J. Chem. Phys.* **2016**, *145*, 149901.
(76) Skomorowski, W.; Krylov, A. I. Feshbach−Fano approach for calculation of Auger decay rates using equation-of-motion coupled-cluster wave functions. I. Theory and implementation. *J. Chem. Phys.* **2021**, *154*, 084124.
(77) Skomorowski, W.; Krylov, A. I. Feshbach−Fano approach for calculation of Auger decay rates using equation-of-motion coupled-cluster wave functions. II. Numerical examples and benchmarks. *J. Chem. Phys.* **2021**, *154*, 084125.
(78) Sorensen, S. L.; Zheng, X.; Southworth, S. H.; Patanen, M.; Kokkonen, E.; Oostenrijk, B.; Travnikova, O.; Marchenko, T.; Simon, M.; Bostedt, C.; Doumy, G.; Cheng, L.; Young, L. From synchrotrons for XFELs: the soft x-ray near-edge spectrum of the ESCA molecule. *J. Phys. B: Atom., Mol. Opt. Phys.* **2020**, *53*, 244011.
(79) Zheng, X.; Cheng, L. Performance of delta-coupled-cluster methods for calculations of core-ionization energies of first-row elements. *J. Chem. Theory Comput.* **2019**, *15*, 4945−4955.
(80) Vidal, M. L.; Krylov, A. I.; Coriani, S. Dyson orbitals within the fc-CVS-EOM-CCSD framework: theory and application to X-ray photoelectron spectroscopy of ground and excited states. *Phys. Chem. Chem. Phys.* **2020**, *22*, 2693−2703.
(81) Vidal, M. L.; Krylov, A. I.; Coriani, S. Correction: Dyson orbitals within the fc-CVS-EOM-CCSD framework: theory and application to X-ray photoelectron spectroscopy of ground and excited states. *Phys. Chem. Chem. Phys.* **2020**, *22*, 3744−3747.
(82) Andersen, J. H.; Nanda, K. D.; Krylov, A. I.; Coriani, S. Probing molecular chirality of ground and electronically excited states in the UV-vis and X-ray regimes: An EOM-CCSD study. *J. Chem. Theory Comput.* **2022**, *18*, 1748−1764.
(83) Zuev, D.; Vecharynski, E.; Yang, C.; Orms, N.; Krylov, A. I. New algorithms for iterative matrix-free eigensolvers in quantum chemistry. *J. Comput. Chem.* **2015**, *36*, 273−284.
(84) Faber, R.; Andersen, J. H.; Coriani, S. py-CCRSP, Python module for CC and EOM-CC response experiments. 2020−2022.
(85) http://iopenshell.usc.edu/resources/howto/symmetry (accessed 2022-07-15).
(86) Mulliken, R. S. Report on notation for the spectra of polyatomic molecules. *J. Chem. Phys.* **1955**, *23*, 1997−2011.
(87) Becke, A. D. Density-functional thermochemistry. III. The role of exact exchange. *J. Chem. Phys.* **1993**, *98*, 5648−5652.
(88) Stephens, P. J.; Devlin, F. J.; Chabalowski, C. F.; Frisch, M. J. Ab initio calculation of vibrational absorption and circular dichroism spectra using density functional force fields. *J. Phys. Chem.* **1994**, *98*, 11623−11627.
(89) Vidal, M. L.; Epshtein, M.; Scutelnic, V.; Yang, Z.; Xue, T.; Leone, S. R.; Krylov, A. I.; Coriani, S. Interplay of open-shell spin-coupling and Jahn-Teller distortion in benzene radical cation probed by X-ray spectroscopy. *J. Phys. Chem. A* **2020**, *124*, 9532−9541.
(90) Schirmer, J.; Trofimov, A. B.; Randall, K. J.; Feldhaus, J.; Bradshaw, A. M.; Ma, Y.; Chen, C. T.; Sette, F. *K*-shell excitation of the water, ammonia, and methane molecules using high-resolution photoabsorption spectroscopy. *Phys. Rev. A* **1993**, *47*, 1136−1147.
(91) Hitchcock, A. P.; Brion, C. E. *K*-shell excitation of HF and F_2 studied by electron energy-loss spectroscopy. *J. Phys. B: At. Mol. Phys.* **1981**, *14*, 4399−4413.
(92) Duflot, D.; Flament, J.-P.; Heinesch, J.; Hubin-Franskin, M.-J. Re-analysis of the *K*-shell spectrum of benzene. *J. Electron Spectrosc. Relat. Phenom.* **2000**, *113*, 79−90.
(93) Coreno, M.; Avaldi, L.; Camilloni, R.; Prince, K. C.; de Simone, M.; Karvonen, J.; Colle, R.; Simonucci, S. Measurement and ab initio calculation of the Ne photoabsorption spectrum in the region of the *K* edge. *Phys. Rev. A* **1999**, *59*, 2494−2497.
(94) Turci, C. C.; Urquhart, S. G.; Hitchcock, A. P. Inner-shell excitation spectroscopy of aniline, nitrobenzene, and nitroanilines. *Can. J. Chem.* **1996**, *74*, 851−869.
(95) Coriani, S.; Christiansen, O.; Fransson, T.; Norman, P. Coupled-cluster response theory for near-edge X-ray-absorption fine structure of atoms and molecules. *Phys. Rev. A* **2012**, *85*, 022507.

https://doi.org/10.1021/acs.jctc.2c00541
J. Chem. Theory Comput. 2022, 18, 6189−6202